



Irradiance and cloud optical properties from solar photovoltaic systems

James Barry^{1,2}, Stefanie Meilinger¹, Klaus Pfeilsticker², Anna Herman-Czezuch¹, Nicola Kimiaie¹, Christopher Schirrmeister¹, Rone Yousif¹, Tina Buchmann², Johannes Grabenstein², Hartwig Deneke³, Jonas Witthuhn³, Claudia Emde⁴, Felix Gödde⁴, Bernhard Mayer⁴, Leonhard Scheck^{4,5}, Marion Schroedter-Homscheidt⁶, Philipp Hofbauer⁷, and Matthias Struck⁷

¹International Centre for Sustainable Development, Hochschule Bonn-Rhein-Sieg, Sankt Augustin

²Institute of Environmental Physics, University of Heidelberg

³Leibniz Institute for Tropospheric Research, Leipzig

⁴Meteorological Institute, Ludwig-Maximilians-Universität München

⁵Hans-Ertel Centre for Weather Research, Munich

⁶German Aerospace Center (DLR), Institute of Networked Energy Systems, Oldenburg

⁷egrid applications & consulting GmbH, Kempten

Correspondence: James Barry (james.barry@iup.uni-heidelberg.de)

Abstract.

Solar photovoltaic power output is modulated by atmospheric aerosols and clouds and thus contains valuable information on the optical properties of the atmosphere. As a ground-based data source with high spatiotemporal resolution it has great potential to complement other ground-based solar irradiance measurements as well as those of weather models and satellites, thus leading to an improved characterisation of global horizontal irradiance. In this work several algorithms are presented that can retrieve global tilted and horizontal irradiance and atmospheric optical properties from solar photovoltaic data and/or pyranometer measurements. Specifically, the aerosol (cloud) optical depth is inferred during clear sky (completely overcast) conditions. The method is tested on data from two measurement campaigns that took place in Allgäu, Germany in autumn 2018 and summer 2019, and the results are compared with local pyranometer measurements as well as satellite and weather model data. Using power data measured at 1 Hz and averaged to 1 minute resolution, the hourly global horizontal irradiance is extracted with a mean bias error compared to concurrent pyranometer measurements of 11.45 W m^{-2} , averaged over the two campaigns, whereas for the retrieval using coarser 15 minute power data the mean bias error is 16.39 W m^{-2} .

During completely overcast periods the cloud optical depth is extracted from photovoltaic power using a lookup table method based on a one-dimensional radiative transfer simulation, and the results are compared to both satellite retrievals as well as data from the COSMO weather model. Potential applications of this approach for extracting cloud optical properties are discussed, as well as certain limitations, such as the representation of 3D radiative effects that occur under broken cloud conditions. In principle this method could provide an unprecedented amount of ground-based data on both irradiance and optical properties of the atmosphere, as long as the required photovoltaic power data are available and are properly pre-screened to remove unwanted artefacts in the signal. Possible solutions to this problem are discussed in the context of future work.



20 1 Introduction

An accurate determination of incoming solar radiation at the Earth's surface is important not only for both climate and weather research, but in future will also be vital for the stable operation of the electricity grid. In Germany alone there are 2.2 million photovoltaic (PV) systems installed, with a nominal power of 60 GWp (Bundesverband Solarwirtschaft e.V., 2021), so that accurate forecasts of solar PV power generation are indeed becoming indispensable for cost-effective grid operation. In this context the proliferation of PV systems provides a unique opportunity to characterise global irradiance with unprecedented spatiotemporal resolution, which would lead to improvements in both weather and climate models. Solar panels can in this way be seen as a dense network of sensors for atmospheric optical properties. This new information could facilitate the development of highly resolved PV power forecasts, as well as play a role in improving climate models, in particular since the highly variable nature of cloud cover as well as uncertainties in cloud microphysics result in the greatest uncertainty in our understanding of the radiative forcing of the climate.

It has been shown by several authors [see for instance Urraca et al. (2018); Ohmura et al. (1998); Frank et al. (2018); Zubler et al. (2011)] that the estimates of global horizontal irradiance (GHI) from both the global ECMWF (ERA5) and regional (COSMO-REA6) numerical weather prediction (NWP) model reanalyses deviate from ground-based measurements. In Urraca et al. (2018), comparisons were made with pyranometer measurements from the Baseline Solar Radiation Network (BSRN) (Ohmura et al., 1998) as well as from a dense network of pyranometers operated by European meteorological services. In general the model reanalyses overestimate the irradiance under cloudy skies, which is largely due to an underestimation of cloud optical depth (COD). The mean positive bias of ERA5 daily mean irradiance is $+4.05 \text{ W m}^{-2}$ (3.47%) over Europe and $+4.54 \text{ W m}^{-2}$ (2.92%) worldwide. On the other hand, the regional COSMO-REA6 data set underestimates GHI on clear sky days, with a mean bias of -5.29 W m^{-2} (-3.22%), which can be attributed to the use of an aerosol climatology with a too large aerosol optical depth (AOD), as discussed in Frank et al. (2018). Although the COSMO-D2 data uses a different aerosol scheme, these negative biases in the GHI are still present, especially in summer (Zubler et al., 2011). Satellite datasets perform a lot better, with data from the Solar surfAce RADIation Heliosat (SARAH) showing a mean bias of only $+0.86 \text{ W m}^{-2}$ in the daily mean GHI (compared to $+4.22 \text{ W m}^{-2}$ from ERA5) over Europe (Urraca et al., 2018). Interestingly SARAH overestimates in most cases, with only some stations showing a negative bias related to snow detection. Overall the satellite measurements display a smaller absolute error than reanalysis products. The positive bias of the GHI from satellite retrievals was confirmed by Yang and Bright (2020): their comprehensive global evaluation of hourly satellite irradiance data reveals a mean bias error¹ of 4.67 W m^{-2} for hourly SARAH-2 irradiance compared to the nine BSRN stations over Europe (excluding the Austrian station Sonnblick at 3100 m altitude), compared to 7.93 W m^{-2} for the Copernicus Atmospheric Monitoring Service (CAMS) radiation data (cf. Section 3.3).

The idea of using PV systems as radiation sensors has been explored by several authors. In Engerer and Mills (2014), Killinger et al. (2016), Marion and Smith (2017), methods are developed in order to use the output of one PV system to predict that of another, which is in essence done by inferring GHI from PV power measurements. In all three cases empirical models

¹Calculated using Table 3 in Yang and Bright (2020).



for the decomposition of irradiance into direct and diffuse components are used, and system parameters such as orientation and PV module efficiency are required inputs. A similar approach is taken in Elsinga et al. (2017), in this case using a single diode PV model and a different decomposition model. In Halilovic et al. (2019) the authors replaced the original iterative approach used in Killinger et al. (2016) by an analytical method, to minimise computational cost. In Nespoli and Medici (2017) a different method is introduced, in this case without the need for system-specific information such as orientation or nominal power. A similar approach is taken in Saint-Drenan (2015); Saint-Drenan et al. (2015), where system parameters are estimated by statistical methods. In addition, Scolari et al. (2018), Laudani et al. (2016), Carrasco et al. (2014) and Abe et al. (2020) have also described the inference of solar irradiance from PV current and voltage measurements using an equivalent circuit model. In this case greater accuracy is achievable, provided the module temperature is also measured.

This work builds upon the proof of concept study presented in Buchmann (2018) (for clear sky days only), however it is unique in that empirical models for the separation of radiation components are avoided – rather an explicit simulation of the diffuse radiance distribution is performed using libRadtran (Mayer and Kylling, 2005; Emde et al., 2016). Although this is computationally more intensive it has several advantages over the usual approach [see for instance Perez et al. (1992)]: by using a state-of-the-art radiative transfer code one can more accurately model the clear sky irradiance, especially for larger solar zenith angles, and one can explicitly take into account information on aerosol load or ground albedo from freely available datasets. In addition it is possible to include information on the state of the atmosphere from weather models, which is particularly relevant in including the effects of precipitable water on incoming irradiance. The radiative transfer solvers DISORT (Stamnes et al., 1988; Buras et al., 2011) and MYSTIC (Mayer, 2009) are used for forward model calibration as well as for inferring atmospheric optical properties and GHI from ground-based irradiance measurements and/or PV power data.

In order for a PV-based determination of solar irradiance to viably complement the global coverage of state-of-the-art satellite measurements, a mean bias error of the order of 5 W m^{-2} would be desirable, which requires precise calibration of the PV systems. The first step is to accurately model the generated power as a function of system-specific parameters, such as the array's elevation and azimuth angle, conversion efficiency and temperature dependence, and then extract those parameters from measured power data using a fitting procedure. In order to remove any biases related to atmospheric conditions, it makes sense to first calibrate the systems under clear skies. Once this has been done to sufficient accuracy one can use measured PV power to infer atmospheric optical parameters such as aerosol or cloud optical depth under different sky conditions, enabling the inference of GHI as well as in some cases of direct and diffuse irradiance components.

The more parameters used to model the PV power, the greater the uncertainty in the retrieved irradiance. For this reason it is of course desirable to obtain as much a priori metadata about the PV systems as possible, such as datasheet parameters and array orientation. However, this information is not always readily available, especially when considering a large amount of PV systems over a wide area. In that sense, there will always be a trade-off between quantity and quality of the data, which then plays itself out in the accuracy of the retrieved irradiance. The advantage of PV systems or any ground-based devices is that one can achieve a much higher spatiotemporal resolution compared to satellite data or weather models, which thus allows one to study high-frequency fluctuations of global irradiance.



In the European context, irradiance variability is dominated by the optical properties of clouds and less by those of aerosols. Ground-based COD retrievals using broadband measurements from pyranometers have been carried out in several studies (see for example Leontyeva and Stamnes (1994); Boers (1997); Boers et al. (1999); Deneke (2002)). Indeed, the transmission of irradiance through a cloud is most sensitive to its optical depth, and less sensitive to droplet radius, single scattering albedo or asymmetry factor (Leontyeva and Stamnes, 1994). In most previous studies the clouds are assumed to be horizontally homogeneous in a plane-parallel atmosphere with 1D radiative transfer, which leads to a bias in the extraction of cloud optical properties, in particular under broken cloud conditions. By neglecting 3D effects, the horizontal transport of photons is not considered, which however plays an important role in real life situations. These 3D effects can for example lead to an enhancement of solar irradiance (Schade et al., 2007), so that the GHI exceeds the clear sky irradiance due to reflected light from the edges of clouds. The inherent four dimensional variability of clouds also complicates the comparison of ground-based and satellite retrievals of cloud properties, since one compares the time average of a point measurement with a spatially averaged quantity.

The goal of this work is to demonstrate that PV systems can indeed be used as ground-based sensors for both GHI as well as to infer the optical properties of the atmosphere, in particular the COD. First results are presented from two measurement campaigns carried out in autumn 2018 and summer 2019 in the Allgäu region in southern Germany, as part of the BMWi-funded project MetPVNet (Meilinger et al., 2021). In Section 2 the forward model and its calibration are discussed, and the inversion methods are outlined in detail. Section 3 provides a detailed description of the data from the measurement campaigns. The results are presented in Section 4, with a focus on both tilted and horizontal irradiance as well as cloud optical depth under overcast skies, and a summary and conclusions are given in Section 5. Further details of the PV modelling aspects and radiative transfer simulation are found in the Appendix.

2 Photovoltaic power model: calibration and inversion

In order to infer local atmospheric optical properties from measured PV data, accurate modelling of both atmospheric radiative transfer as well as PV power generation is required. In this section both the PV model as well as the libRadtran radiative transfer model is described, along with the calibration and inversion procedure.

2.1 Forward model: from atmospheric properties to photovoltaic power

The power generated by a solar PV module depends primarily on incoming short wave solar irradiance and module temperature, both of which depend on atmospheric conditions. Once this dependence is properly described in a model, PV power and/or current measurements can be used to infer the irradiance in the plane of the array, taking into account the geometry of the system, i.e. the elevation and azimuth angle of the solar panels. After extracting this “global tilted irradiance” (GTI) from PV data, one can go on to infer atmospheric optical properties such as cloud optical depth and global horizontal irradiance, by further inverting the radiative transfer model.

The most physically correct method of modelling the power output of a PV plant is with an equivalent circuit model that captures the properties of semiconductors, such as the two-diode model (see for instance Mertens (2014)). In this way the



temperature dependence of current and voltage is explicitly defined according to the Shockley equation (Shockley, 1949). A
120 drawback of such models is their computational complexity and reliance on parameters found on module datasheets, which are
in the most general case not always available. There are however several parameterised models in the literature that attempt
to reduce the power generation equation to a simple relation between incoming plane-of-array irradiance, module area and
temperature-dependent efficiency, with the latter described as a function of ambient conditions. Several such models exist
(see Skoplaki and Palyvos (2009) for a review), with some of the most popular being that of the “PV Performance Modeling
125 Collaborative” from Sandia National Laboratories (King et al., 2004, 2007) or the Huld model used in the online PVGIS tool
(Huld et al., 2011). Since the goal here is an inversion, the choice of model depends on the availability of measured data: in
this work and in the context of the AC power data from the MetPVNet campaign, a simplified parametric power model is
employed. The model is described here briefly, and more details are given in Appendix A.

In order to correctly capture the effects of the variable solar spectrum one also needs to take into account the spectral
130 response of the PV technology in question (Alonso-Abella et al., 2014), which in the case of an equivalent circuit model can
then be included in the calculation of the photocurrent [see for instance the libRadtran-based spectral PV model described
in Herman-Czezuch et al. (2022)]. In the case of parametrised PV power models, this so-called “spectral mismatch”, i.e., the
difference between the entire spectrum of incoming radiation and the range utilised by a certain PV module, is usually simply
absorbed into the PV model parameters, leading to a site-specific bias that may not take into account variations in the spectrum
135 from local atmospheric conditions. By using libRadtran for calibration and inversion along with information on the state of
the atmosphere from weather models one can take these variations into account in the radiative transfer (RT) simulation and
subsequent inversion, as discussed in 2.2 below. In particular the water vapour column and aerosol optical depth at each site
need to be taken into account (see Section A3 in the Appendix).

It can be shown using the diode model [see for instance Sauer (1994); Abe et al. (2020)] that the maximum power point
140 (MPP) current generated by a PV module is linearly dependent on the incident irradiance, and only very weakly dependent on
temperature. However, the dependence of MPP voltage on temperature (which itself is a function of irradiance) is an order of
magnitude greater (roughly -0.4 %/K), so that this simple linear relationship breaks down when considering the PV power. In
this work a parameterised power model was used [see Buchmann (2018), Skoplaki and Palyvos (2009), as well as Dows and
Gough (1995)], with AC PV power described as²

$$145 P_{AC,mod} \simeq G_{tot,PV,\tau}^{\angle} (b_1 + b_2 G_{tot,SW,\tau}^{\angle} + b_3 T_{ambient} + b_4 v_{wind} + b_5 T_{sky}), \quad (1)$$

in the case of the linear temperature model defined in Eq. (A3) (TamizhMani et al., 2003), or as

$$P_{AC,mod} \simeq G_{tot,PV,\tau}^{\angle} \left(b'_1 + \frac{G_{tot,SW,\tau}^{\angle}}{b'_2 + b'_4 v_{wind}} + b'_3 T_{ambient} + b'_5 T_{sky} \right), \quad (2)$$

in the case of the non-linear temperature model defined in Eq. (A4) (Faiman, 2008; Barry et al., 2020). This means that the
modelled AC power $P_{AC,mod}$ is a non-linear function of plane-of-array irradiance $G_{tot,PV,\tau}^{\angle}$, together with the effects of am-
150 bient temperature $T_{ambient}$, wind speed v_{wind} and sky temperature T_{sky} that influence module temperature and thus efficiency.

²The inverter efficiency is included in the parameter s , see Section A in the Appendix.



Note that $G_{\text{tot,PV},\tau}^{\angle}$ represents the part of the irradiance that contributes to the photovoltaic effect, whereas $G_{\text{tot,SW},\tau}^{\angle}$ refers to all incoming shortwave photons. The parameters $b_i(b'_i)$, ($i = 1 \dots 5$) depend on nominal power, efficiency, the temperature coefficient for power as well as the temperature model parameters, and are discussed in more detail in Appendix A, which includes a list of all parameters in Table 2. In practice the module temperature can either be measured or modelled, depending
155 on the availability of measurements and/or meteorological data.

Within the PV power models described in Eqs. (1) and (2), the PV module temperature is a static quantity, i.e., the heat capacity (C) of the PV system is not taken into account. However, when dealing with high-frequency measurements of PV power it is necessary to employ a dynamic temperature model, as discussed in Barry et al. (2020). The characteristic time constant ($= C/J$, with J the net thermal energy flux of the PV modules) of typically 10 minutes means that the large fluctu-
160 ations in irradiance do not translate directly to module temperature variations, i.e. the temperature response is smoothed out. For simplicity the dynamic temperature model was not included in the present study, since most of the systems had power data collected in 15 minute resolution.

The subscript “PV” for the tilted irradiance $G_{\text{tot,PV},\tau}^{\angle}$ in Eqs. (1) and (2) refers to the fact that only the relevant wavelength (in this case 300 nm to about 1200 nm for silicon PV modules) is considered, and the subscript “ τ ” indicates that transmission
165 through the glass surface of the PV panels has been taken into account with an optical model. Further details of the model employed here are given in Sections A1 and A2 in the Appendix, and the refractive index n of the glass covering is one of the parameters varied in the optimisation procedure. The dependence of the spectral mismatch on atmospheric water vapour will be discussed in Section 2.3.

2.2 Model calibration under clear sky conditions

170 In order to infer the irradiance in the plane-of-array (GTI) from measured PV power or current, the PV model parameters need to be determined, either from datasheets or with a forward model calibration. This is accomplished using data under clear sky conditions, together with an accurate simulation of the irradiance, followed by a multi-parameter optimisation to find the parameter values. This section describes the technical details of the clear sky simulation and the relevant atmospheric input parameters used. Figure 1 displays this procedure graphically, and further explanations are given in the following sections.

175 2.2.1 Radiative transfer simulation with libRadtran

The clear sky simulation of tilted irradiance $G_{\text{tot,PV},\tau}^{\angle}$ is performed with the freely available libRadtran software package (Mayer and Kylling, 2005; Emde et al., 2016), with the input parameters shown in Table 1 and the wavelength range 300 nm to 1200 nm for silicon PV applications. The corresponding broadband simulation ($G_{\text{tot,SW},\tau}^{\angle}$) is also performed, as an input to the temperature model. Spectral integration is carried out using the Kato parameterisation, in order to simplify the
180 effects of water vapour absorption by using the so-called correlated-k approximation (Kato et al., 1999). The DISORT solver allows for an explicit calculation of the diffuse radiance distribution on a predefined lattice of elevation and azimuth angles, and the pseudospherical approximation is employed, so that only radiative transfer calculations at solar zenith angles (SZA) of up to 80 degrees can be reliably performed. The Python package `PyEphem` (Rhodes, 2022) is used to accurately determine

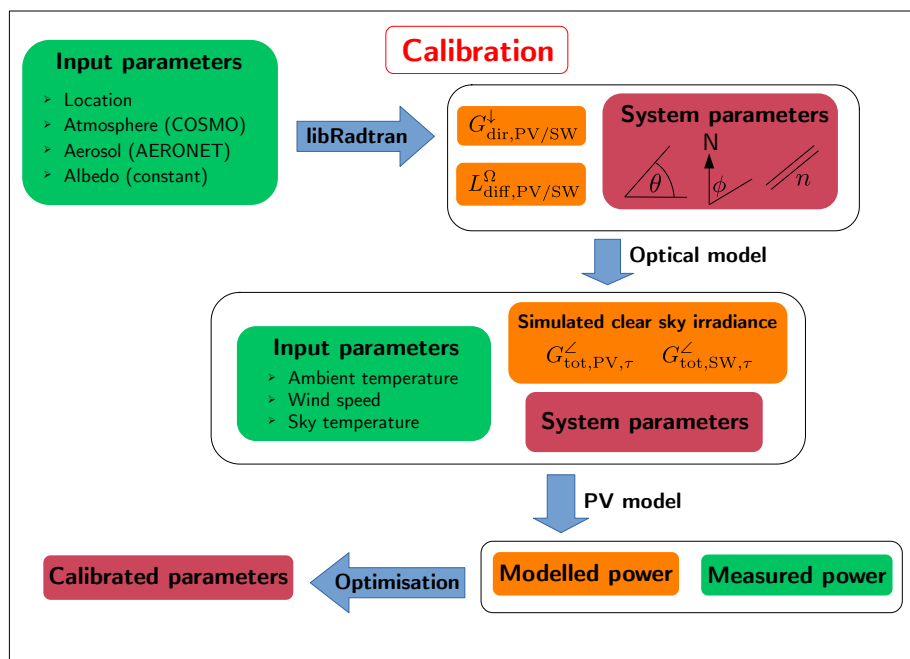


Figure 1. Schematic diagram showing the different steps of the calibration procedure, with input data sources in green, model steps/algorithms in blue, simulated parameters in orange and system parameters (cf. Table 2) in dark red. Note that in this case only clear sky days or time periods are considered.

Table 1. Model parameters for libRadtran simulation of clear sky days, including information on their source.

Parameter	Symbol	Source
Latitude, longitude, altitude, time	φ, ϑ, z, t	Set by PV data
Solar zenith angle, solar azimuth angle	θ_0, ϕ_0	Calculated with PyEphem (Rhodes, 2022)
Temperature profile	$T(z)$	COSMO (Baldauf et al., 2011)
Pressure profile	$p(z)$	COSMO
Water vapour	$[H_2O](z)$	COSMO
Ozone	$[O_3](z)$	US standard atmosphere
Albedo	$\rho(\lambda)$	Constant (0.2)
Ångström turbidity coefficient	$\tau_{a,1}$	AERONET (Holben et al., 1998)
Ångström exponent	α	AERONET
Other aerosol optical properties	-	OPAC “continental average” (Hess et al., 1998)



the sun position for the corresponding latitude, longitude, time coordinates. COSMO model data (see Section 3.2) are interpo-
185 lated by the package `cosmomystic` (see software supplement) in both time and space in order to create atmosphere profile
files suitable as input for `libRadtran`, in 15 minute resolution. In this way variations in water vapour and other atmospheric
trace gases are taken into account, and the atmospheric layers are cut off at the appropriate altitude of each site. Concurrent
measurements by an AEROSOL ROBOTIC NETWORK (AERONET) sun photometer (Holben et al., 1998) are used to extract the
Ångström exponent α and turbidity coefficient $\tau_{a,1}$ with the `aeronetmystic` (see software supplement) software package.
190 Other aerosol optical properties such as the single scattering albedo and asymmetry factor are taken from the Optical Properties
of Aerosols and Clouds (OPAC) species library with the option “continental average” (see Table 3 in Hess et al. (1998)).

In order to speed up the simulation the code is parallelised to run on multiple processors: the simulation times are divided
up into batches and `libRadtran` is then called multiple times as a subprocess from Python. In this way the clear sky simulation
takes approximately 1 second per time step (8 seconds on an 8 core machine), using a diffuse radiance field of 5° resolution in
195 both elevation and azimuth angle, atmosphere files modified from COSMO data and modified aerosol inputs from AERONET
and OPAC.

2.2.2 Non-linear optimisation for PV system parameters

The simplified parametric model described above can be written as

$$P_{AC,mod} \equiv \mathbf{y} = \mathbf{F}(\mathbf{x}, \mathbf{h}), \quad (3)$$

200 for the forward model \mathbf{F} described by Eq. (A1) and state space defined by (cf. Table 2)

$$\mathbf{x} \equiv (\theta, \phi, n, s, \zeta, u_i), \quad (4)$$

so that the calibration procedure is effectively a non-linear, multi-parameter optimisation problem with eight (for the non-
linear temperature model)³ or nine (for the linear temperature model) unknowns. As shown in Table 3, the parameter space
 \mathbf{h} in Eq. (3) contains the irradiance proxy from the `libRadtran` simulation as well as temperature and wind speed data from
205 either the COSMO model or measurements, which were interpolated to 15 minute resolution. In addition the measured sky
temperature (see Section 3.1) was used. This inversion problem can be solved with the methods detailed in Rodgers (2000). In
this case the Levenberg-Marquardt algorithm was used, with the Jacobian matrix calculated explicitly at each iteration.

If one varies all parameters in \mathbf{x} it quickly becomes apparent that there are not enough degrees of freedom in the signal to
uniquely determine a solution with the Bayesian formalism, since several parameters are highly correlated with each other, for
210 instance the inclination angle θ with the scaling factor s , or the orientation angle ϕ with the temperature model parameters or
the coefficient ζ (cf. the discussion in Section 4.1). It is thus expedient to extract the temperature model parameters separately
using measured module temperature for different PV system configurations (if available) and then fix those parameters in the
optimisation procedure. In Barry et al. (2020) a dynamic model was developed by fitting the measured and modelled module

³In the non-linear Faiman model there are less temperature parameters as the ambient and sky temperatures are not independent, as is the case in the linear
model, cf. Eqs. (A3) and (A4).



Table 2. List of PV model parameters in \boldsymbol{x} . In the calibration procedure, those parameters in \boldsymbol{x} known to a certain degree (from datasheets or other sources) of accuracy were fixed, whereas all others were varied.

Parameter (\boldsymbol{x})	Symbol	Source (if available)
Tilt angle	θ	laser scanning and/or theodolite
Azimuth angle	ϕ	laser scanning and/or theodolite
Glass refractive index	n	optimisation
Scaling factor	s	optimisation
Temperature coefficient	ζ	datasheet and/or optimisation
Temperature model parameters	$u_i (i = 0, 1, 2, 3)$	optimisation and/or model (Barry et al., 2020)

Table 3. List of additional inputs in \boldsymbol{h} used for calibration on clear sky days. The subscripts “PV” and “SW” refer to the different wavelength bands used for integration, see the discussion in Section 2.2.1.

Parameter (\boldsymbol{h})	Symbol	Source
Direct tilted irradiance	$G_{\text{dir,PV(SW)}}^{\angle}$	libRadtran simulation (see Table 1)
Diffuse tilted irradiance	$G_{\text{diff,PV(SW)}}^{\angle}$	libRadtran simulation (see Table 1)
2m ambient temperature	T_{ambient}	COSMO and/or measured
Wind speed at 10m	v_{wind}	COSMO and/or measured
Longwave downward welling irradiance	$G_{\text{LW}}^{\downarrow}$	measured

temperature using three different PV systems with different mountings. These results (for the static model case) were used in
 215 the overall optimisation, where appropriate.

The calibration algorithm is designed to allow certain parameters to be fixed if they are known, whereas unknown parameters are varied with a given a priori error, which in turn affects the parameter retrieval error and thus propagates into the uncertainty in the inferred irradiance.

2.3 Model inversion under all sky conditions

220 The calibrated PV systems can now be used as sensors to extract information about the state of the atmosphere. This section describes the different methods used to infer both irradiance and atmospheric optical properties from PV power data, as summarised in the schematic diagram in Figure 2. The method employed depends on the prevailing weather conditions, specifically on the amount (and type) of cloud cover. In a nutshell, using a 1D DISORT-based method one can use GTI to extract AOD or COD during clear or completely overcast periods, respectively, which thus allows the determination of the direct and diffuse
 225 irradiance components. Under broken cloud conditions, a 3D MYSTIC-based method allows one to determine the GHI from GTI directly. The DISORT and MYSTIC lookup tables (LUTs) are provided in an open data repository.

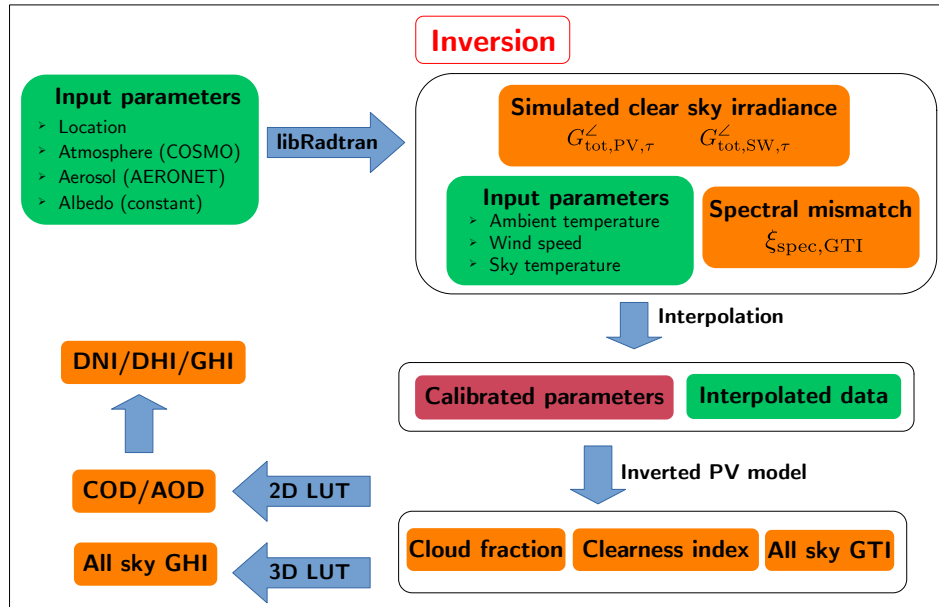


Figure 2. Schematic diagram showing the different steps of the inversion procedure, with input data sources in green, model steps/algorithms in blue, simulated/retrieved parameters in orange and system parameters in dark red. Note that in this case all atmospheric conditions (all sky) are considered.

2.3.1 Global tilted irradiance from PV model inversion

Once the PV system has been calibrated under clear sky conditions, the system parameters can be fixed and the measured PV power can be used to infer the global tilted irradiance (GTI, also denoted as $G_{\text{tot,SW}}^{\angle}$) under all sky conditions. The temperature model makes use of broadband irradiance [see Eqs. (1) and (2)], whereas the PV power model uses only the relevant spectral range of silicon PV modules (300 nm-1200 nm), so that the spectral mismatch between the light converted to electricity ($G_{\text{tot,PV},\tau}^{\angle}$) and the entire shortwave spectrum needs to be taken into account when inverting the model chain.

The ratio of PV-relevant ($G_{\text{tot,PV}}^{\angle}$) to broadband ($G_{\text{tot,SW}}^{\angle}$) tilted irradiance is a function of system geometry, time of day as well as local atmospheric conditions, with the largest contributing factor being the precipitable water in the atmosphere. In order to take this into account the libRadtran clear sky irradiance simulations (see Section 2.2.1) were used to characterise the ratio

$$\xi_{\text{spec,GTI}} \equiv \frac{G_{\text{tot,PV},\tau}^{\angle}}{G_{\text{tot,SW},\tau}^{\angle}} = f(\Theta, [\text{H}_2\text{O}], \text{AOD}), \quad (5)$$

as a function of incident angle Θ , precipitable water and aerosol optical depth, for each station and measurement campaign. In this way the available information on water vapour column and aerosol extinction from the COSMO model and AERONET can



240 be taken into account in the PV model inversion. Details are given in Section A3 in the Appendix. The fitting function could in principle be extended to include ozone column abundance, which was however not included here, since this information was not available from the COSMO model data. Note that although this method does not take into account the effect of clouds on the spectral mismatch it is a good first approximation, which will be improved upon in future work (see also Rivera Aguilar and Reise (2020) for an alternative method). In addition one could modify this algorithm to include operational satellite retrievals
 245 of atmospheric parameters such as ozone concentration, if required.

Once the spectral mismatch factor $\xi_{\text{spec,GTI}}$ has been calculated, the next step is to extract the plane-of-the-array irradiance from PV power, which in the case of the models given in Eqs. (1) and (2) is simply the solution to the quadratic equations in $G_{\text{tot,SW},\tau}^{\angle}$, i.e.,

$$\xi_{\text{spec,GTI}} b_2 (G_{\text{tot,SW},\tau}^{\angle})^2 + (b_1 + b_3 T_{\text{ambient}} + b_4 v_{\text{wind}} + b_5 T_{\text{sky}}) \xi_{\text{spec,GTI}} G_{\text{tot,SW},\tau}^{\angle} - P_{\text{AC,meas}} = 0, \quad (6)$$

250 for the linear temperature model and

$$\frac{\xi_{\text{spec,GTI}}}{(b_2 + b_4 v_{\text{wind}})} (G_{\text{tot,SW},\tau}^{\angle})^2 + (b_1 + b_3 T_{\text{ambient}} + b_5 T_{\text{sky}}) \xi_{\text{spec,GTI}} G_{\text{tot,SW},\tau}^{\angle} - P_{\text{AC,meas}} = 0, \quad (7)$$

for the non-linear temperature model. These equations can be solved with the quadratic formula, using the calibrated parameters $b_{1,2,3,4,5}$ ($b'_{1,2,3,4,5}$) as defined in Eq. (A5) (Eq. (A6)) for the linear (non-linear) temperature model, the available data for T_{ambient} , v_{wind} and T_{sky} as well as the spectral mismatch factor for GTI defined in Eq. (5). Note that the inverted $G_{\text{tot,SW},\tau}^{\angle}$
 255 is the irradiance impinging upon the PV module under the glass covering, so that the optical model has not yet been inverted. In order to compare this quantity with pyranometers, the transmission of light through the glass $\tau_{\text{PV,rel}}(\Theta)$ [also known as “incidence angle modifier”, see Eq. (A9)] must be taken into account, so that the final GTI is given by [see also Eq. (A15)]

$$G_{\text{tot,SW}}^{\angle} = \frac{G_{\text{tot,SW},\tau}^{\angle}}{\tau_{\text{PV,rel,eff}}}. \quad (8)$$

For the direct extraction of GTI an empirical formulation is used to find the effective incidence angle for the diffuse component,
 260 whereas for the inversion onto optical properties the refractive index is explicitly taken into account within the radiative transfer simulation. More details are given in Section A2 in the Appendix.

2.3.2 Clearness index and irradiance variability classification

Using the global tilted irradiance extracted from measured PV power data, different methods are used in order to extract atmospheric optical properties and global horizontal irradiance, depending on the prevailing weather conditions. By combining
 265 the inverted tilted irradiance with the corresponding clear sky curve one can calculate a clearness index

$$k_i(t) = \frac{G_{\text{tot,SW},\tau,\text{inv}}^{\angle}(t)}{G_{\text{tot,SW},\tau,\text{clear}}^{\angle}(t)} \quad (9)$$

for each time step, allowing the data to be separated into clear, overcast and broken cloud time periods. The clearness index is then used to estimate the cloud fraction, which will be discussed in more detail in Section 2.3.3.



On clear days (or during clear time periods) the aerosol optical depth (AOD) can be inferred, whereas under cloudy condi-
270 tions the cloud optical depth (COD) can be found, depending on the degree of cloud cover. In this work the extraction of COD
using a DISORT-based LUT under completely overcast skies is examined in more detail in Section 2.3.3. An in-depth analysis
of aerosol optical properties will be carried out in future work. For broken cloud conditions, a MYSTIC-based LUT was used
to infer the global horizontal irradiance from tilted irradiance measurements, as discussed in Section 2.3.5 [see Chapter 9 of
Meilinger et al. (2021)].

275 2.3.3 Cloud optical depth with DISORT lookup table

Cloud optical properties are functions of microphysical properties such as droplet size distribution, droplet number concen-
tration as well thermodynamic phase. For water clouds, the absorption and scattering of solar irradiance can be efficiently
characterised (Hu and Stamnes, 1993) by the effective radius r_{eff} and cloud liquid water content (LWC), which can be related
to cloud optical depth (COD, τ_c) through

$$280 \quad \tau_c = \frac{3 \text{LWP}}{2 r_{\text{eff}} \rho_{\text{H}_2\text{O}}}, \quad (10)$$

where the liquid water path (LWP) is the integral of the LWC across the height of the cloud. Although both τ_c and r_{eff}
can be accurately retrieved from spectral measurements of reflected radiation, the transmission of light through clouds is
mostly sensitive to the cloud optical depth. This is due to the fact that changes in transmission due to variations in single
scattering albedo and asymmetry factor (which depend on r_{eff}) are small compared to those due to changes in optical depth
285 (Leontyeva and Stamnes, 1994). For illustration, in the two stream approximation for conservative scattering (no absorption),
the transmittance T can be shown to be [see for instance Petty (2006)]

$$T = \frac{1}{1 + (1 - g) \tau_c}, \quad (11)$$

where g is the asymmetry factor. For liquid water clouds, scattering is mostly in the forward direction, with $g \simeq 0.85$, whereas
for ice clouds $g \simeq 0.7$. In both cases the variations in g are small, so that τ_c is the primary factor influencing T . The hyperbolic
290 dependency of T on τ_c means that the transmission curve is rather steep at small optical depths, but flattens out for $\text{COD} \gtrsim 15$.
This has implications for the accuracy of ground-based retrievals, as will be discussed in detail in Section 4.4. It must also be
noted that in the algorithm described in Section 2.3.1, spectral variations in cloud optical properties are not taken into account.
In practice this means that variations in the single scattering albedo at higher wavelengths around $1 \mu\text{m}$ (silicon PV modules
are still sensitive to wavelengths up to $1.2 \mu\text{m}$) may be unaccounted for.

295 In this work a lookup table for the optical depth of a typical stratus cloud is constructed using DISORT in 15 minute time
intervals, under the assumption of a pseudospherical or plane-parallel atmosphere with horizontally homogeneous liquid water
clouds and a completely cloudy sky. This means that 3D effects are not taken into account and the results need to be interpreted
with care, especially in situations with broken clouds. In addition, different cloud types such as thicker cirrus clouds, mixed
phase or multi-layer clouds are not properly represented by the LUT. Due to the pseudospherical approximation only SZA
300 up to 75° are considered (for SZA above 75° with cloud cover the pseudospherical DISORT solver is unstable). The cloud



Table 4. Cloud parameters for the DISORT simulation of a continental stratus cloud (Hess et al. (1998)).

Cloud parameter	Value
Liquid water content (LWC)	0.28 g m ⁻³
Effective radius (r_{eff})	7.33 μm
Cloud height (h)	1 – 2 km

parameters in Table 4 are input into libRadtran and the COD at 550 nm ($\tau_{c,550\text{nm}}$) is varied on a 16 step logarithmic scale between COD = 0.5 and COD = 150, using the default “hu” parameterisation (Hu and Stamnes, 1993) and 16 streams.

As described for the clear sky simulation in Section 2.2 the direct irradiance and diffuse radiance field are calculated with libRadtran, the latter in this case with a coarser resolution of 10 degrees in both azimuth and elevation angles.⁴ The LUT is then used to find the COD by first calculating the plane-of-array irradiance for the corresponding PV system or pyranometer orientation (cf. Section 2.3.1) and then interpolating the COD in time to match the resolution of the measured data. For this purpose the original 1 Hz pyranometer and PV data were smoothed to 1 minute resolution, whereas the low frequency PV data was kept at 15 minute resolution (see Section 3.1).

In order to determine the exact time points at which a cloud is above the sensor, the cloud fraction is determined by creating a mask based on the clearness index in Eq. (9) using a threshold of 0.8 and overshoot limit of 1.1, i.e.,

$$cf(t) = \begin{cases} 1 & \text{if } k_i(t) \leq 0.8 \\ 0 & \text{if } 0.8 < k_i(t) \leq 1.1 \\ \text{nan} & \text{if } k_i(t) > 1.1 \end{cases} \quad (12)$$

This binary cloud mask (clear = 0, cloudy = 1) is then also smoothed with a moving average function over 60 minutes in order to create an estimate of the cloud fraction ($\langle cf \rangle_{60}$) for comparison with cloud camera measurements. The COD is then only extracted for data points for which $cf(t) = 1$, i.e. by finding the values of $\tau_{c,550\text{nm}}$ for which

$$G_{\text{tot},\text{SW},\text{meas}/\text{inv}}^{\angle} = G_{\text{dir},\text{SW},\text{cloudy}}^{\angle}(\tau_{c,550\text{nm}}) + G_{\text{diff},\text{SW},\text{cloudy}}^{\angle}(\tau_{c,550\text{nm}}), \quad (13)$$

for all points under a cloud, where “meas” or “inv” refer to measured or inverted GTI from pyranometers or PV systems, respectively. The corresponding direct and diffuse components can then also be extracted from the LUT, although in this case the direct irradiance is basically zero (beneath a cloud).

As mentioned above, this approach is limited by the fact that a 1D radiative transfer solver such as DISORT cannot take into account horizontal transport of photons, so that 3D effects such as radiative enhancement under broken cloud conditions [see for instance Schade et al. (2007)] are not taken into account. For this reason only situations with overcast conditions will be

⁴Note that for more accurate radiance calculations one could use the “mie” option in libRadtran, which uses pre-calculated tables for Mie scattering and is however computationally more expensive.



considered when applying this method. In situations with low overall cloud cover, the COD is not the main determinant of the total irradiance received by the sensor or PV system, but rather the cloud fraction and/or the AOD. To this end a complementary approach using a MYSTIC-based LUT (see Section 2.3.5) was used, in order translate measured tilted irradiance to horizontal irradiance under broken cloud conditions.

2.3.4 Aerosol optical depth with DISORT lookup table

As mentioned above, in this work the extraction of the AOD will not be discussed in detail. However the procedure will be briefly described here, since this is used as an alternative method for determining the GHI from tilted irradiance measurements. An AOD-GTI lookuptable can be created in a similar way to the COD LUT described in Section 2.3.3, where in this case the AOD at 500nm is varied on a logarithmic scale in 16 steps between AOD = 0.01 and AOD = 1. In addition, the aerosol properties are fixed to the so-called “continental average” scheme from the OPAC database Hess et al. (1998). In this way, the AOD can be extracted on clear sky days, and thus the direct and diffuse irradiance as well as the global horizontal irradiance.

In Germany and especially in the Allgäu region the AOD is however very small (almost always lower than 0.5), so that any errors in the calibration procedure lead to large relative biases in the AOD. This then leads to biases in the direct and diffuse components, but since there are very few absorbing aerosols, these errors have opposite signs and largely cancel out in the determination of the GHI. In Section 4, the GHI extracted via both COD and AOD under different conditions will be compared to that measured by pyranometers and satellites, as well as the GHI predicted by the COSMO weather model. However the inferred AOD itself will be not be examined in detail.

2.3.5 From tilted to horizontal irradiance with MYSTIC lookup table

In order to extract the global horizontal irradiance from the tilted irradiance (from pyranometers or PV systems) a MYSTIC-based LUT for the GHI was developed using LES cloud fields Črnivec and Mayer (2019), taking into account various factors such as albedo, water vapour, sensor geometry and cloud fraction. Detailed 3D radiative transfer simulations were carried out and the most important factors turn out to be simply the sensor and sun geometry as well as the cloud fraction, which reflects the fact that a pyranometer or PV system sees the entire sky. A detailed description of the MYSTIC LUT is given in Chapter 9, Section 9.1.5 of Meilinger et al. (2021).

The measured or inverted tilted irradiance, together with the average cloud fraction over the last hour (as described above) is fed into the MYSTIC LUT, along with the sensor and sun geometry. In this way the GHI can be extracted from the GTI under broken cloud conditions. This method can however not be used to determine the optical depth, nor can the direct and diffuse irradiance components be separated from each other, since the fit was created using the GTI and GHI.



Table 5. Dates of clear sky days during the measurement campaigns in autumn 2018 and summer 2019.

1st campaign	12 Sept 2018	17 Sept 2018	20 Sept 2018	27 Sept 2018	30 Sept 2018	4 Oct 2018
	5 Oct 2018	8 Oct 2018	10 Oct 2018	12 Oct 2018	13 Oct 2018	14 Oct 2018
2nd campaign	26 Jun 2019	27 Jun 2019	28 Jun 2019	29 Jun 2019	30 Jun 2019	4 Jul 2019
	23 Jul 2019	24 Jul 2019	25 Jul 2019			

350 3 Measurement and validation data

3.1 Ground-based measurements

Model calibration and inversion was performed with PV power data recorded over two measurement campaigns in autumn 2018 and summer 2019, as part of the MetPVNet measurement campaign [see Chapter 3 of Meilinger et al. (2021)]. There were a total of 24 stations spread out in the region around Kempten (47.715924°N, 10.314006° E), as shown in Figure 3, with
355 22 of them equipped with silicon-based pyranometers measuring both GHI and GTI in the plane-of-array of the PV system. Two master stations (MS01 and MS02) were also equipped with secondary standard pyranometers and pyrhemometers in order to measure both components of the incoming short wave radiation, cloud cameras as well as spectrometers to record spectral information. The station MS01 also contained a sun photometer to determine aerosol properties, as part of AERONET, as well as a pyrgeometer to measure longwave downwelling irradiance.

360 The PV power data was for the most part provided by the local distribution network operator Allgäuer Überlandwerk GmbH (AÜW), recorded in 15 minute intervals. These data represent the amount of energy generated in the last 15 minutes, so that care needs to be taken to translate them into a measured power corresponding to a specific time stamp. For this purpose the data were simply shifted by half a period and resampled, since by integration of power over 15 minutes one effectively smooths the power curve. In addition there were five stations equipped by egrid GmbH with high frequency power measurement devices:
365 for these stations the power was recorded in 1 Hz resolution.

Analysis of the measured data revealed a total of twelve clear sky days that occurred between 12 September 2018 and 14 October 2018, as well as nine clear sky days between 25 June 2019 and 13 August July 2019, as shown in Table 5. COSMO model data for the corresponding days was procured from Germany's National Meteorological Service, the Deutscher Wetterdienst (DWD), in order to accurately recreate atmospheric conditions using `cosmomystic`. These days were used for
370 calibration of each PV system.

The network of PV systems was equipped with low cost silicon-based pyranometers, with two devices per station: one mounted in the plane of the PV array and one horizontal, with 1 Hz resolution and an overall accuracy of 5%. These sensors had been absolutely calibrated at the Leibniz Institute for Tropospheric Research (TROPOS) prior to the campaign, by comparing their output to that of a secondary standard pyranometer (2% accuracy). In order to compensate for errors in mounting the
375 plane-of-array pyranometers, the calibration algorithm described in 2.2 was also applied to the pyranometer data, in this case without an optical model and only using data up to a SZA of 60 degrees. Due to the substantial cosine bias, a correction factor

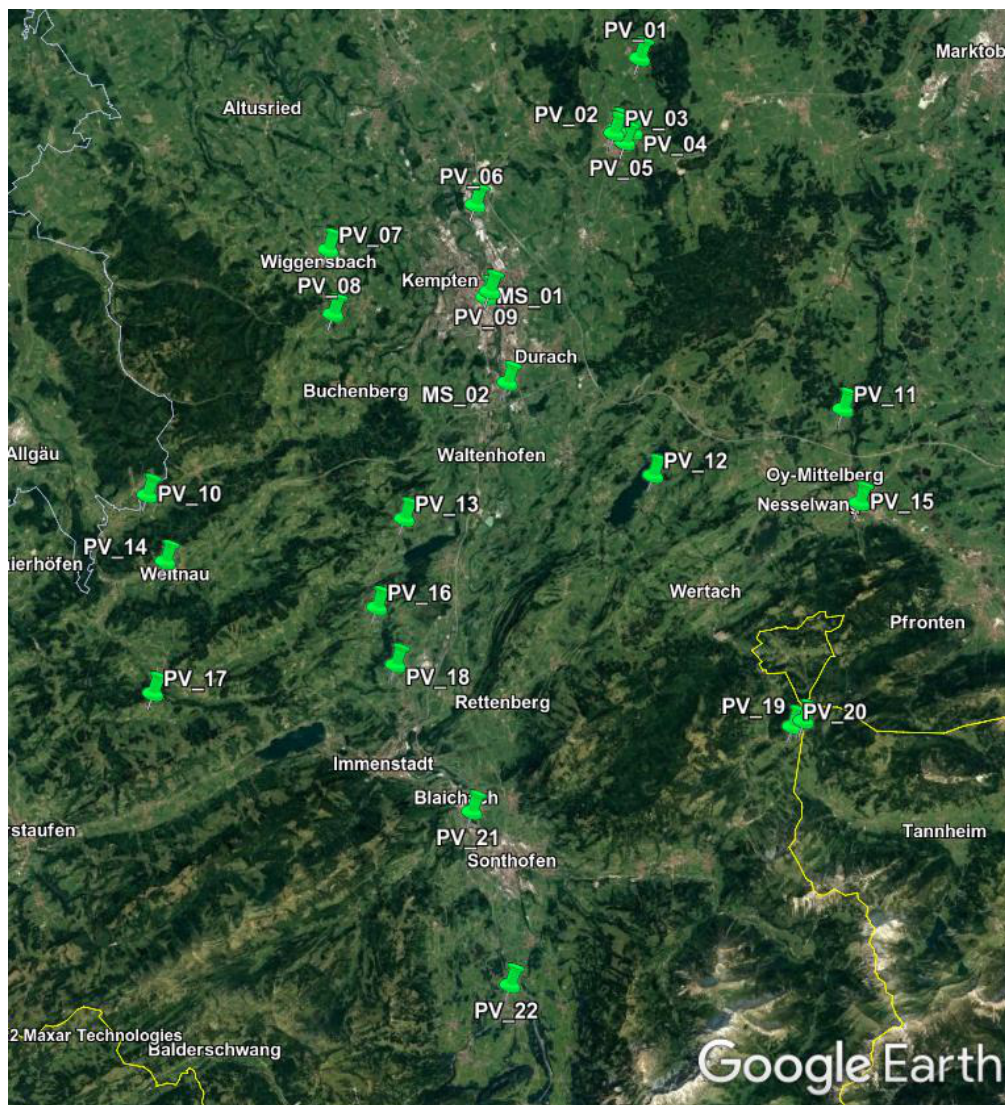


Figure 3. Map showing locations of PV systems used in the MetPVNet measurement campaign (taken from © Google Earth). The top left corner is at 47.85° N, 10.09° E, the bottom right corner at 47.38° N, 10.52° E. The yellow line marks the border between Germany and Austria; the grey line is the border between the states of Bavaria and Baden-Württemberg.

was empirically determined:

$$C(\mu) = -3.01\mu^3 + 5.59\mu^2 - 3.34\mu + 1.45 \quad (14)$$

where $\mu = \cos\theta_0$ for horizontal sensors and $\mu = \cos\Theta$ for tilted sensors (θ_0 is the SZA and Θ the angle of incidence, see Eq. A8). The pyranometer data was used for comparison with the inverted irradiance (both tilted and horizontal), as well as for finding atmospheric optical properties using the lookup table method.



3.2 Weather model data

The Consortium for Small-Scale Modelling (COSMO) numerical weather model is a nonhydrostatic regional model developed by the DWD (Baldauf et al., 2011). Note that this model was recently replaced by the so-called ICOSahedral Nonhydrostatic (ICON) model, which has been fully operational since January 2021. In this work the COSMO-EU model with a spatial resolution of 2.2km was used, both as input to the clear sky irradiance simulation (see Section 2.2.1), for PV model calibration (see Section 2.2.2) as well as for validation and/or comparison of the inverted irradiance with weather model predictions. For the clear sky simulation, temperature and pressure profiles as well as the water vapour column was extracted from COSMO data, whereas for both the calibration and inversion procedure the surface temperature and wind speed were used. For comparison and validation both direct and diffuse downward irradiance data was used.

For comparison with the cloud optical depth extracted from the PV systems, the COSMO model COD for both liquid water and ice clouds was combined into a total COD, using a cloud overlap scheme to add up $\tau_{c,w}$ and $\tau_{c,i}$ in each subcolumn, and this sum was averaged over 5×5 grid boxes centred around the grid box closest to the relevant ground station.

3.3 Satellite data

The Copernicus Atmospheric Monitoring Service (CAMS) radiation service (Qu et al., 2017; Schroedter-Homscheidt et al., 2022) is an online satellite and numerical model-based service with radiation, cloud and aerosol data available for free download, covering the period from February 2004 to the present. The spatial coverage is Europe/Africa/Middle East/Eastern part of South America/Atlantic Ocean, interpolated to the point of interest, and with a time resolution of up to 1 minute. In this work the global, direct and diffuse components of irradiance were imported from CAMS (version 4.0), for each station and for all days in the two measurement campaigns. These data were used as a comparison for the irradiance inverted from PV systems.

In addition to irradiance, CAMS provides data on cloud and aerosol properties. In this work, the cloud parameters from the AVHRR (Advanced Very High Resolution Radiometer) Processing scheme Over cLOUDs, Land and Ocean Next Generation (APOLLO_NG) analysis (Kriebel et al., 2003; Klüser et al., 2015) were used, using data from the Spinning Enhanced Visible and InfraRed Imager (SEVIRI) instrument on board the Meteosat Second Generation (MSG) satellite. In this case the so-called Stephens method (Stephens et al., 1984) is used to determine the COD, using a two-stream solution of the radiative transfer equation, along with an updated algorithm using a probabilistic approach for cloud detection (Klüser et al., 2015). For comparison with the COD inferred from the PV systems, APOLLO_NG data was extracted for the closest pixel to each station.

4 Results

The calibration and inversion procedure described in Section 2 was applied to the data from the measurement campaign described in Section 3 in order to extract irradiance and optical properties from the PV systems in the Allgäu region. After a brief summary of the calibration results in Section 4.1, the retrievals of tilted and horizontal irradiance are presented in Sections 4.2 and 4.3, and the inferred COD results are shown in Section 4.4.



4.1 Model calibration and uncertainty

The PV models in Eqs. (1) and (2) were used together with the clear sky simulation described in Section 2.2.1 and the clear sky days (in Table 5) in order to calibrate each system. In each individual case those days that turned out not to be clear were discarded from the calibration dataset, and the data was restricted to those time periods in which the required inputs such as ambient temperature, atmospheric longwave irradiance and wind speed were available. In order to validate the calibration results the retrieved elevation and azimuth angles were compared to ground truth data from the Bavarian Agency for Digitisation, High-Speed Internet and Surveying (LDBV). The so-called “Level of Detail 2” (LoD2) database contains a 3D building model constructed using airborne laser scanning, so that the roof pitch of individual buildings can be extracted. Figure 4 shows a comparison of the retrieved orientation angles with the ground truth values, for each system and using the linear temperature model.

In most cases the algorithm finds reasonable values for the angles: the larger deviations can usually be explained individual cases, for instances for PV04 the inverter MPP tracking algorithm distorts the clear sky days, whereas for the systems at PV11 the different PV arrays at the site were not well characterised. In other cases shading effects played a role: in most cases the calibration performed better when using both summer and autumn data, since in summer the sun is much higher and shading effects play a smaller role. In general the model calibration works best when using as much data as possible, since one has for instance more variation in temperature in order to find more reliable temperature model parameters.

As discussed in Section 2.2.2, several parameters are correlated with each other: the size of the PV system (captured by the factor s) correlates with the tilt angle θ , whereas the azimuth angle ϕ shows a large correlation with the parameters of the temperature model, since the warming up and cooling down of the PV system is delayed with respect to the diurnal variation of solar irradiance. In general the use of measured module temperature leads to better calibration results. It turns out that the calibration algorithm presented here doesn't perform well using the non-linear Faiman temperature model and 15 minute power data, even though this model couples irradiance and windspeed in a more physically correct way [see for instance Faiman (2008); Barry et al. (2020)]. The benefit of this model is lost for coarsely resolved 15 minute data, so that in the end the algorithm proposed here does not always find an optimal solution, specifically if the temperature model parameters are unknown. The bias that then occurs in the final inversion results can be seen in the plots in Section B in the Appendix as well as in the results in Tables 7, 8, 10, 11 and 12 in the following sections. Table 6 lists the PV systems used in this work, along with the corresponding time resolution of their data.

4.2 Global tilted irradiance from PV power data

In this section the plane-of-array irradiance from PV power retrievals is compared to the tilted pyranometer measurements at selected stations during the two measurement campaigns. The results were obtained using two different approaches for module temperature: (i) the linear temperature model [Eq. (A3)], and (ii) the non-linear Faiman temperature model [Eq. (A4)]. The results are compared in Tables 7 and 8 in the main text, and scatter plots using the linear model are also shown, whereas plots using the Faiman model are shown in the Appendix. Both stations with 15 minute power data as well as those with high

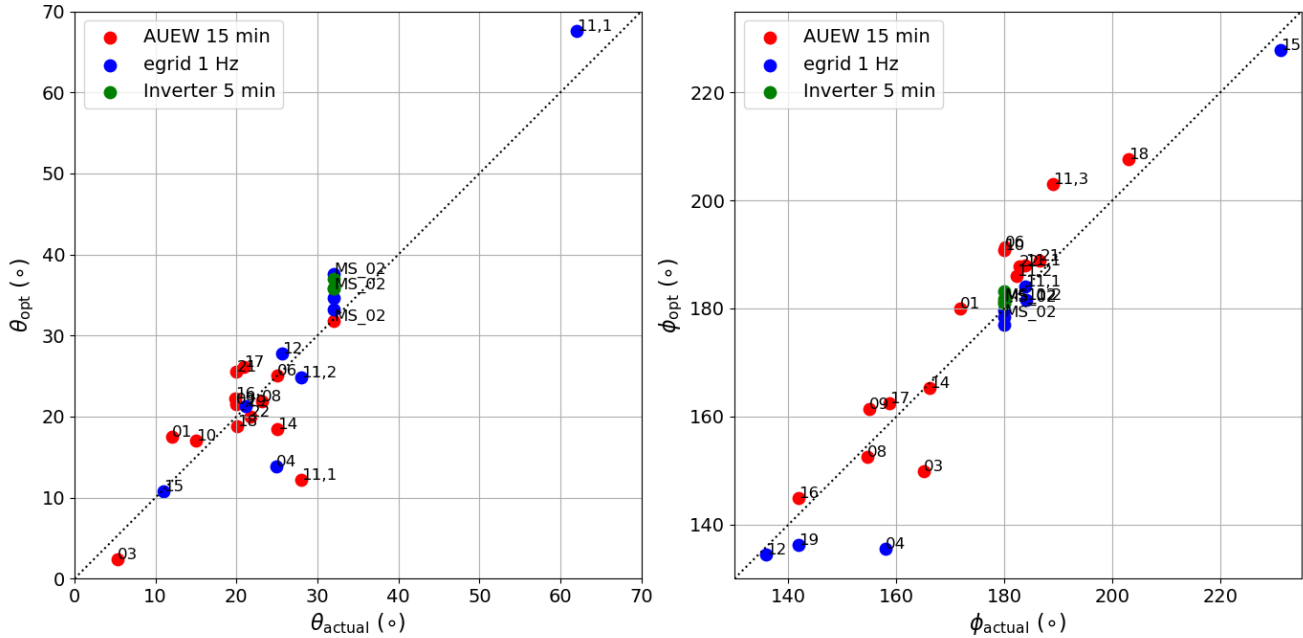


Figure 4. Comparison of retrieved azimuth (elevation) angle ϕ_{opt} (θ_{opt}) with ground truth (ϕ_{actual} and θ_{actual}) from airborne laserscanning data.

frequency data (1 Hz data, smoothed to 1 minute resolution) are included in the analysis, and in each case a comparison is made to the measurements from TROPOS silicon-based pyranometers, except for the master station MS02, where the tilted Kipp&Zonen CMP11 pyranometer is used for validation.

Figures 5 and 6 show a comparison between the retrieved GTI and that measured by pyranometers, for the 1 minute and 450 15 minute data respectively, for each measurement campaign and using the linear temperature model. The same results for the Faiman temperature model are shown in figures B1 and B2. The corresponding statistical measures of mean bias error (MBE), defined by

$$MBE = \frac{1}{n} \sum_{i=1}^n (X_{inv} - X_{ref}), \quad (15)$$

as well as root mean squared error (RMSE), defined by

$$RMSE = \sqrt{\frac{1}{n} \sum_{i=1}^n (X_{inv} - X_{ref})^2}, \quad (16)$$

for the inverted quantities X_{inv} and the reference quantities X_{ref} are shown in Tables 7 and 8. The scatter plots throughout this work are coloured according to a probability density function calculated using the multi-variate gaussian kernel density function “gaussian_kde” in the Python toolbox scipy, with yellow (light grey) for high and blue (dark grey) for low frequency



Table 6. List of PV systems used for this work (see also the map in Fig. 3). The data resolution column indicates whether a particular system was used for this analysis or not, with an explanation given in case the system was omitted. Note that stations MS01 and PV02 had no PV systems, only pyranometers and other measurement equipment. PV11 has four separate PV systems.

Station	Data resolution		Mounting	Comments
	2018	2019		
MS02	15 min	15 min / 1 s	Ground	
PV01	15 min	15 min	Rooftop	
PV03	-	-	Rooftop	Calibration errors
PV04	-	-	Rooftop	Calibration errors
PV05	-	-	Rooftop	No data
PV06	15 min	15 min	Ground	
PV07	-	-	Rooftop	Calibration errors
PV08	15 min	-	Rooftop	No data in 2019
PV09	-	-	Rooftop open	Caibration errors
PV10	15 min	15 min	Ground	
PV11,1	15 min	1 s	Rooftop	
PV11,2	15 min	15 min	Rooftop	
PV11,3	15 min	15 min	Rooftop	
PV11,4	1 s	-	Ground	No data in 2019
PV12	1 s	1 s	Rooftop	
PV13	-	-	Rooftop	No 2018 data, calibration problems
PV14	15 min	15 min	Rooftop open	
PV15	1 s	1 s	Rooftop	
PV16	15 min	15 min	Rooftop	
PV17	15 min	15 min	Rooftop	
PV18	15 min	15 min	Rooftop	
PV19	1 s	1 s	Rooftop	
PV20	-	-	Rooftop	No data
PV21	15 min	15 min	Rooftop	
PV22	-	-	Rooftop	Calibration errors

points in the colour (black and white) version. In Figs. 5 and 6 one can see that most points lie close to the 1:1 line, for both
 460 campaigns, albeit with a positive bias in all cases. The 1 minute data shows a larger spread of points than the 15 minute data,
 since in the former case there are more outliers caused by i) temperature effects, ii) 3D radiative transfer effects, and iii) spatial
 effects due to differences in cloud cover and sensor position between PV and pyranometer. In addition the slightly different
 geometry of flat PV arrays compared to glass dome-shaped pyranometers could play a role, especially when it comes to their

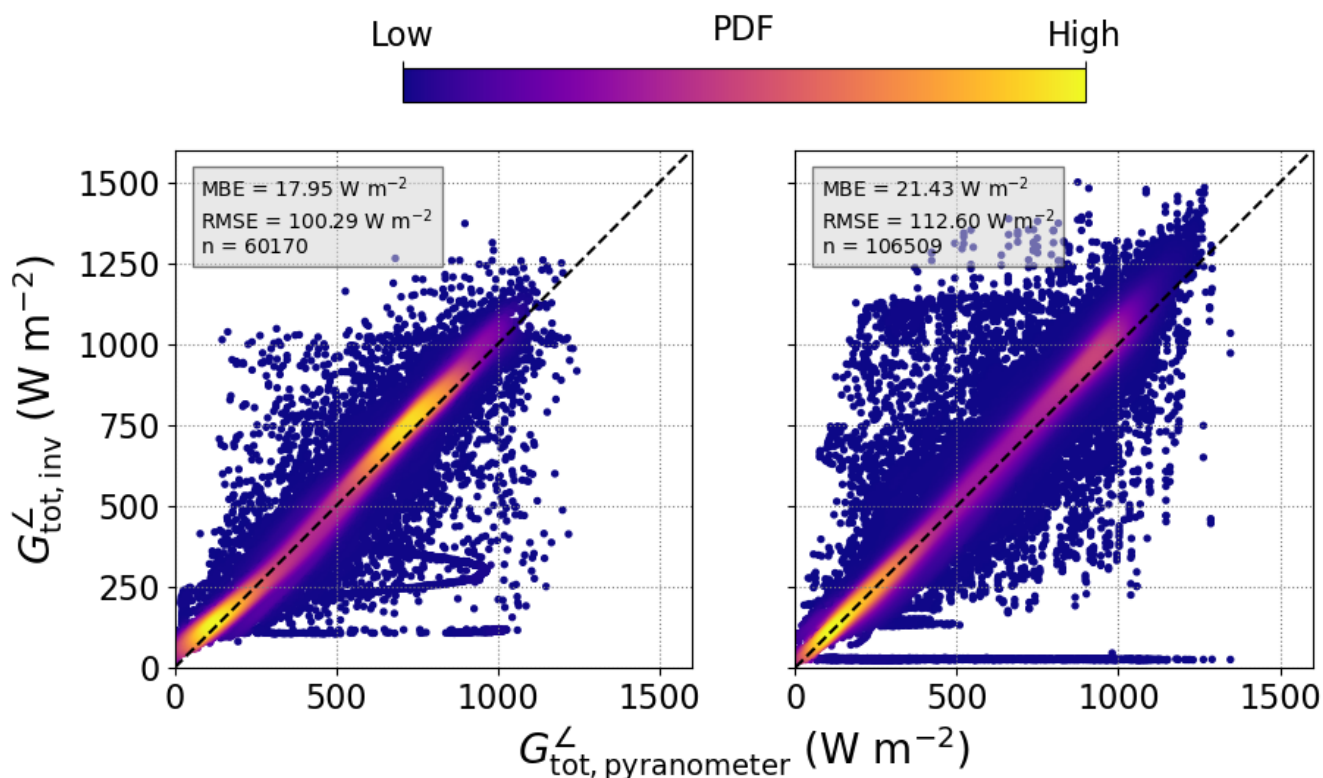


Figure 5. Combined comparison of GTI retrieved from PV power measurements with that measured by tilted pyranometers, using data in 1 minute resolution from MS02, PV11, PV12, PV15, PV19 (cf. Table 6), for 2018 (left) and 2019 (right), together with the linear temperature model [see Eq. (A3)]. Mean bias error (MBE) and root mean squared error (RMSE) are shown in the inset, along with the number of data points used, denoted as n .

sensitivity to different viewing angles. Another possible reason for the positive bias could be a systematic bias in the tilted
 465 pyranometer measurements, even after the bias correction described in Section 3.1.

Note that the results using the Faiman temperature model with 15 minute data (see the values marked with * in Tables 7 and 8) show relatively large bias errors (see Fig. B2 in Appendix B), which has to do with the calibration algorithm not finding an optimal solution for some of the plants.

4.3 Global horizontal irradiance from PV power data

470 In the following the global tilted irradiance (GTI) retrievals are converted to global horizontal irradiance (GHI) and compared to the measurements from pyranometers as well as to the satellite and weather model data. The GTI is converted to GHI in two different ways, depending on the prevailing weather conditions, as described in Section 2.3. In the first case, the DISORT-based LUT is used to find the value of aerosol or cloud optical depth under completely clear or completely overcast conditions,

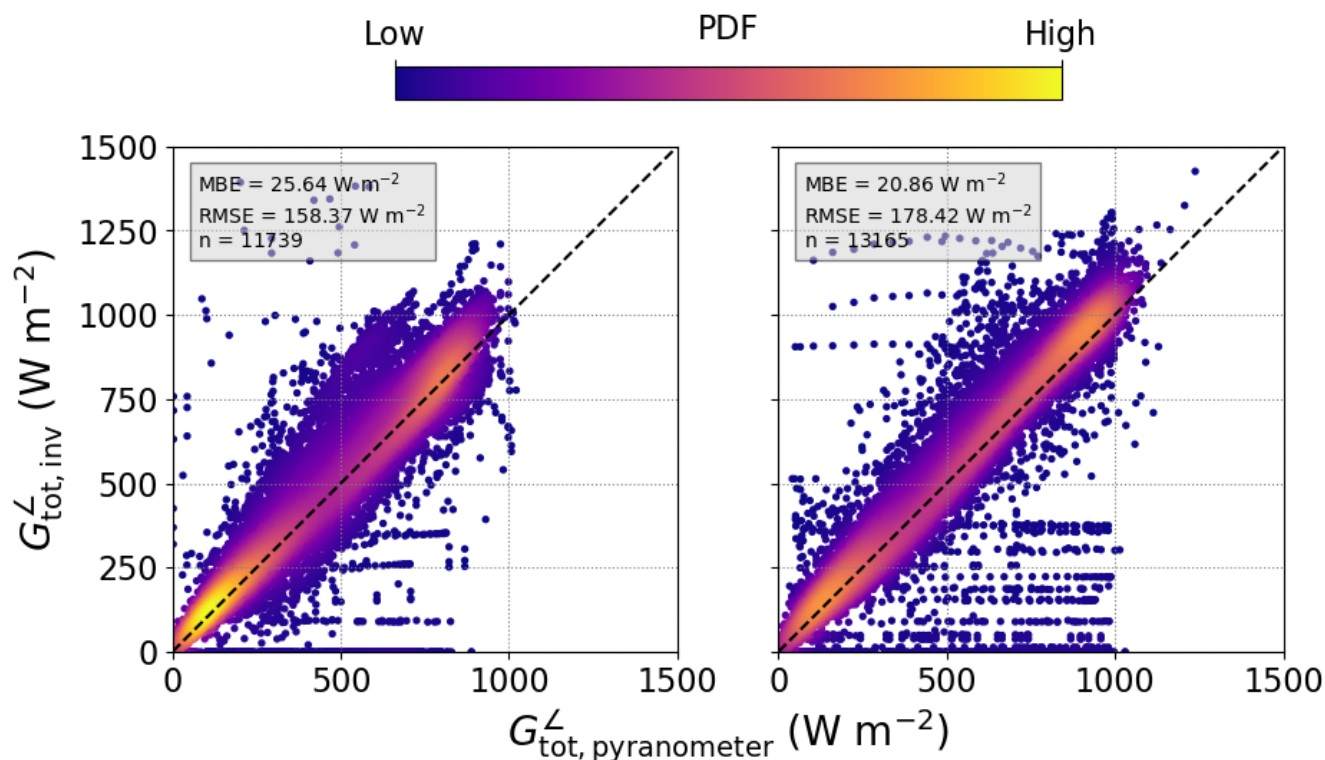


Figure 6. Same as Fig. 5 using data in 15 minute resolution from MS02, PV01, PV06, PV08, PV10, PV11, PV14, PV16, PV17, PV18, PV21 (cf. Table 6) for 2018 (left) and 2019 (right).

Table 7. Mean bias error (in W m^{-2}) of GTI retrievals, compared to tilted pyranometers.

	2018		2019	
	Linear	Faiman	Linear	Faiman
1min	17.95	7.38	21.43	13.44
15min	25.64	89.51*	20.86	84.82*

475 respectively. The inferred AOD/COD is then used to calculate the direct and diffuse irradiance components, which result in the GHI.

The second approach to finding the GHI is using the MYSTIC-based LUT described in Section 2.3.5, where the input parameters to the LUT are simply array geometry, sun position and cloud fraction. In this case there are certain restrictions on these parameters, as shown in detail in Table 9. This means that not all of the retrieved GTI data points can be transformed into GHI using this method – in particular the SZA is limited to between 20° and 60° , and the cloud fraction to between 0.13 and



Table 8. Root mean squared error (in W m^{-2}) of GTI retrievals, compared to tilted pyranometers.

	2018		2019	
	Linear	Faiman	Linear	Faiman
1min	100.29	104.23	112.60	115.50
15min	158.37	231.24*	178.42	266.88*

Table 9. Limits on the input parameters for the MYSTIC LUT.

Input parameter	Limits
SZA (θ_0)	$[20^\circ, 60^\circ]$
Tilt angle (θ)	$[0^\circ, 50^\circ]$
Relative azimuth ($ \phi - \phi_0 $)	$[0^\circ, 90^\circ]$
Cloud fraction	$[0.13, 0.82]$

480 0.82, so that neither completely overcast nor clear sky conditions are taken into account. This method thus deals with the case of mixed/broken cloud conditions, in which there are more likely to be errors due to 3D effects and sensor position.

4.3.1 GHI retrieval validation with pyranometer measurements

The DISORT LUT method performs comparably well for extracting GHI from PV power measurements, which is to be expected considering that it is only employed in stable (clear or cloudy) atmospheric conditions. Figure 7 shows the results for the linear temperature model, for both 1 and 15 minute data (top and middle rows) as well as with data averaged over an hour (bottom row). Note that this plot combines the GHI retrieved under clear skies and completely cloudy skies via the AOD and COD, respectively. The same results for the Faiman temperature model are shown in Fig. B3.

The statistical measures of the different retrievals are shown in Tables 10 and 11. The mean bias error reaches the goal of 5 W m^{-2} only in certain cases. Once again, due to calibration problems the Faiman model shows a large bias for 15 minute data (marked with *), as discussed in Section 4.1. In general one would expect the algorithm to perform better under more stable weather conditions in autumn 2018, however this is not always the case, which can be attributed either to a) cosine bias (even after bias correction) in the pyranometers on clear sky days or b) errors in the calibration, which increase the mean bias error. That the bias may come from temperature effects is further corroborated by the good performance of the Faiman model using 1 minute data. The larger fluctuations of irradiance under broken cloud conditions in the summer campaign lead in general to a larger RMSE, however the bias error in summer is mostly smaller than in autumn.

In the case of the MYSTIC LUT and for the linear temperature model, the retrieved GHI shows a comparatively large bias error, as shown in Figs. 8 for the 1 minute (top row) and 15 minute data (middle row), respectively. On the other hand, the Faiman temperature model performs better here, especially for the 1 minute data, as seen in the top row of Fig. B4. In both

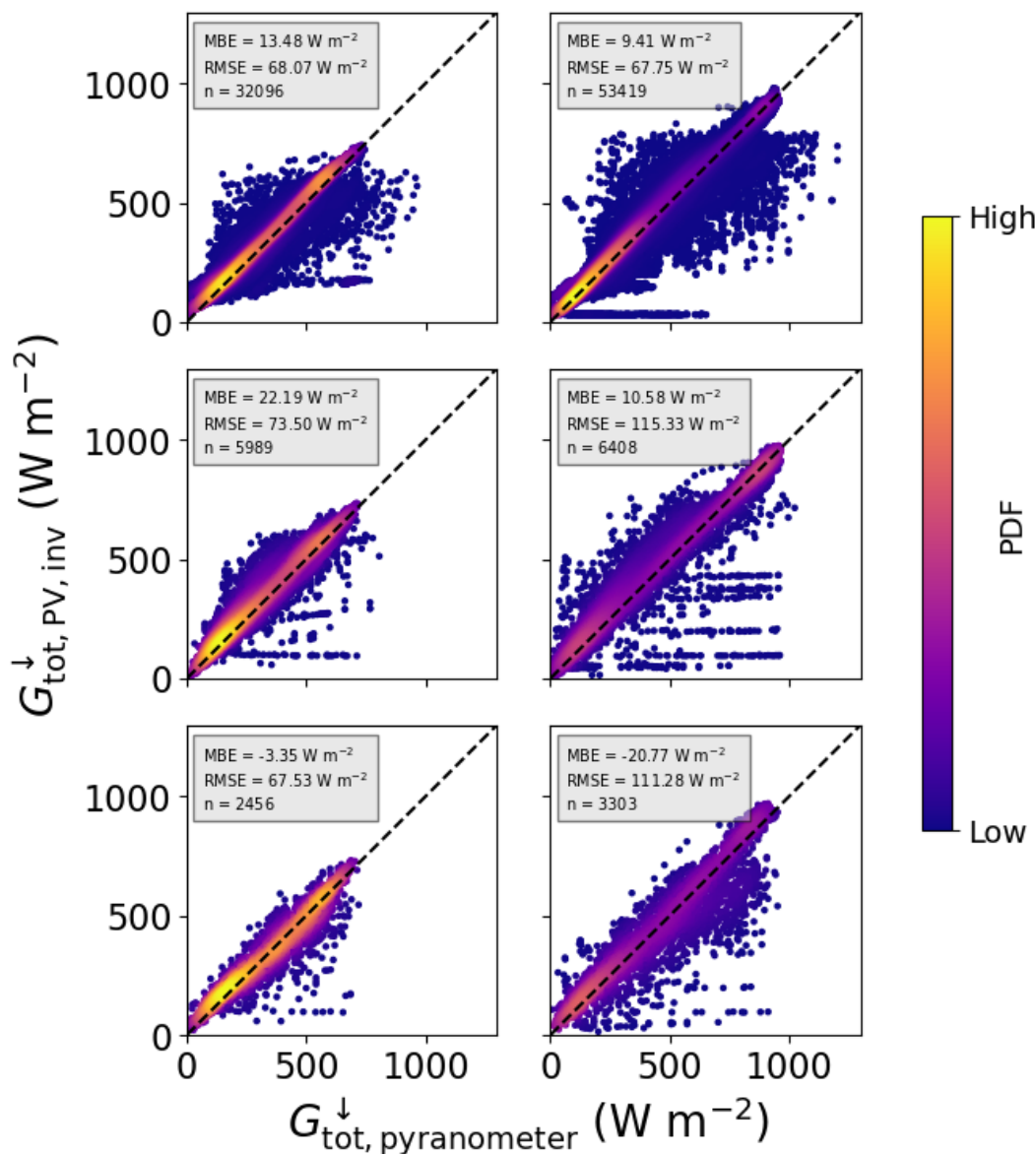


Figure 7. Combined comparison of GHI retrieved from PV power measurements under clear or completely cloudy conditions using the optical depth via DISORT 1D LUT with that measured by horizontal pyranometers, using data in 1 minute resolution (top row) from MS02, PV11, PV12, PV15, PV19, in 15 minute resolution from MS02, PV01, PV06, PV08, PV10, PV11, PV14, PV16, PV17, PV18, PV21 (middle row) and averaged to 60 min (bottom row) for all stations, for 2018 (left) and 2019 (right), using the linear temperature model.

cases, the 15 minute data shows a large bias, and one reason for this could be an incorrect determination of the cloud fraction due to insufficient data, i.e. coarse resolution.



Table 10. Mean bias error (in W m^{-2}) of GHI retrievals using DISORT (1D OD LUT) and MYSTIC (3D LUT), compared to both horizontal pyranometers and CAMS.

	Inversion	Pyranometer				CAMS			
		2018		2019		2018		2019	
		Linear	Faiman	Linear	Faiman	Linear	Faiman	Linear	Faiman
1min data	1D OD LUT	13.48	5.90	9.41	4.81	-18.05	-25.28	-67.66	-69.36
	3D LUT	29.90	0.83	21.19	5.44	45.89	17.35	44.11	29.63
15min data	1D OD LUT	22.19	25.87*	10.58	7.70*	-4.55	-2.34*	-23.75	-26.71*
	3D LUT	47.44	67.69*	48.46	65.73*	48.02	64.63*	54.96	71.98*
60min average	1D OD LUT	-3.35	-3.16	-20.77	-26.33	-10.69	-11.46	-46.30	-50.33
	3D LUT	60.63	70.13	58.98	59.25	56.59	65.42	56.52	58.11

Table 11. Root mean squared error (in W m^{-2}) of GHI retrievals, compared to both horizontal pyranometers and CAMS.

	Inversion	Pyranometer				CAMS			
		2018		2019		2018		2019	
		Linear	Faiman	Linear	Faiman	Linear	Faiman	Linear	Faiman
1min data	1D OD LUT	68.07	68.89	67.75	70.80	95.79	95.51	148.19	148.99
	3D LUT	89.76	87.98	113.09	120.05	206.97	191.99	242.66	237.02
15min data	1D OD LUT	73.50	75.84*	115.33	117.47*	68.38	70.22*	122.54	126.11*
	3D LUT	100.17	128.52*	105.42	142.34*	125.40	149.23*	162.59	186.27*
60min average	1D OD LUT	67.53	70.06	111.28	112.04	70.54	72.08	123.90	125.97
	3D LUT	96.39	119.99	98.41	116.52	109.60	124.92	135.63	148.19

4.3.2 Comparison to satellite and weather model irradiance data

One of the main aims of this work is to show that PV systems can provide a reliable source of information on global horizontal irradiance that is complementary to that from satellite and weather models. Figure 9 shows the comparison between GHI retrieved from PV power using the cloud and aerosol optical depth and that from the CAMS retrieval (see also statistical measures in Tables 10 and 11), for 13 stations and both measurement campaigns, whereas the comparison with COSMO model data is shown in Fig. 10, in both cases with the linear temperature model. For the latter comparison the data was averaged over a 60 minute period. It is evident that the COSMO model shows a bias under clear sky conditions: here the assumed AOD is too high so that the irradiance turns out to be too small. On the other hand, under cloudy conditions and especially under low light conditions in summer the irradiance from COSMO is larger than that retrieved from PV plants, which means that the COD is

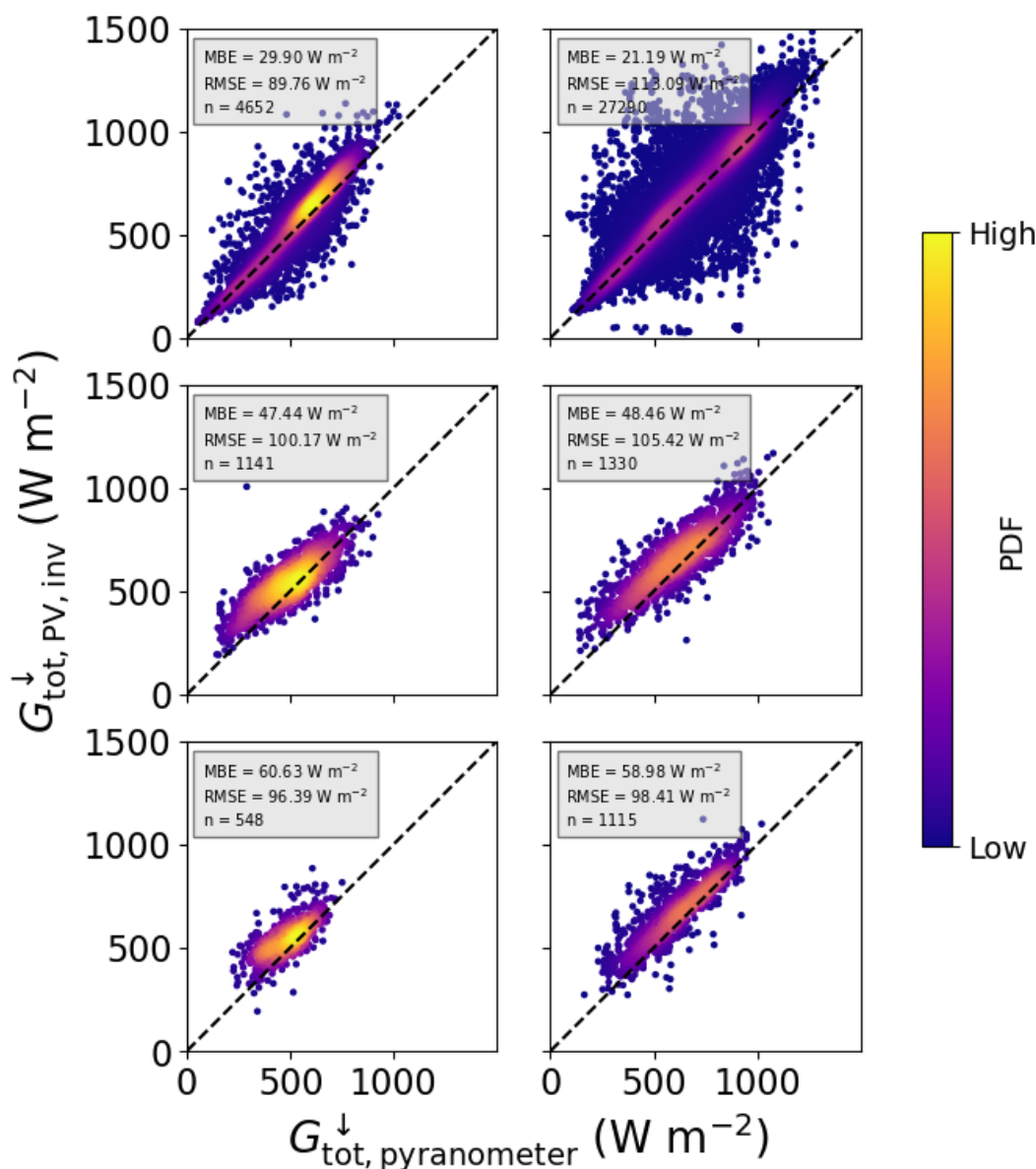


Figure 8. Combined comparison of GHI retrieved from PV power measurements under broken cloud conditions using the MYSTIC LUT with that measured by horizontal pyranometers, using data in 1 minute resolution (top row) from MS02, PV11, PV12, PV15, PV19, in 15 minute resolution from MS02, PV01, PV06, PV08, PV10, PV11, PV14, PV16, PV17, PV18, PV21 (middle row) and averaged to 60 min (bottom row) for all stations, for 2018 (left) and 2019 (right), using the linear temperature model.

510 too small. These results confirm the findings of Frank et al. (2018); Zubler et al. (2011), and are discussed further in connection with the cloud optical depth in Section 4.4 below.

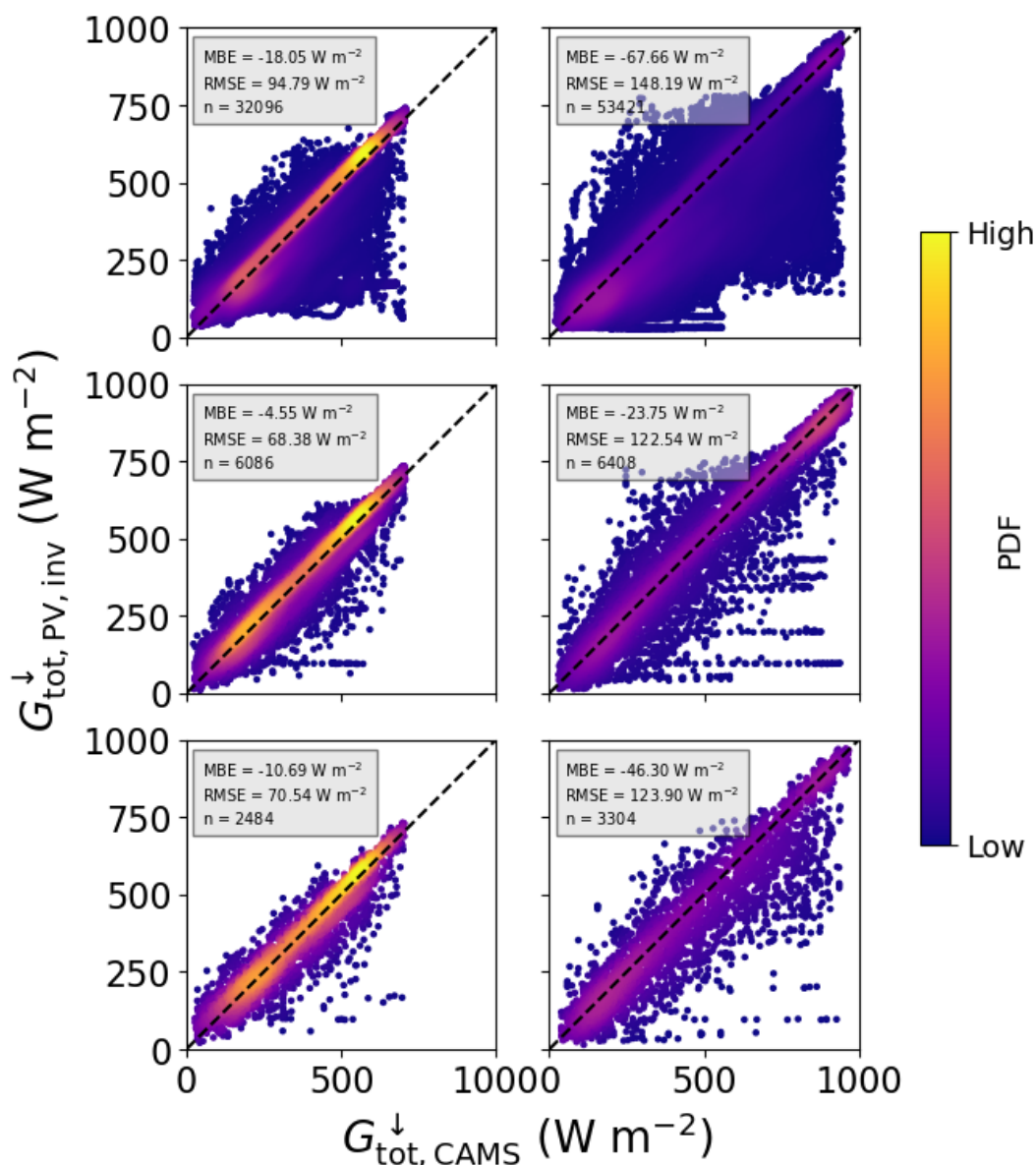


Figure 9. Combined comparison of GHI retrieved from PV power measurements under clear or completely cloudy conditions using the optical depth inferred via DISORT LUT with that from CAMS, using data in 1 minute resolution (top row) from MS02, PV11, PV12, PV15, PV19, in 15 minute resolution from MS02, PV01, PV06, PV08, PV10, PV11, PV14, PV16, PV17, PV18, PV21 (middle row) and averaged to 60 min (bottom row) for all stations, for 2018 (left) and 2019 (right), using the linear temperature model.

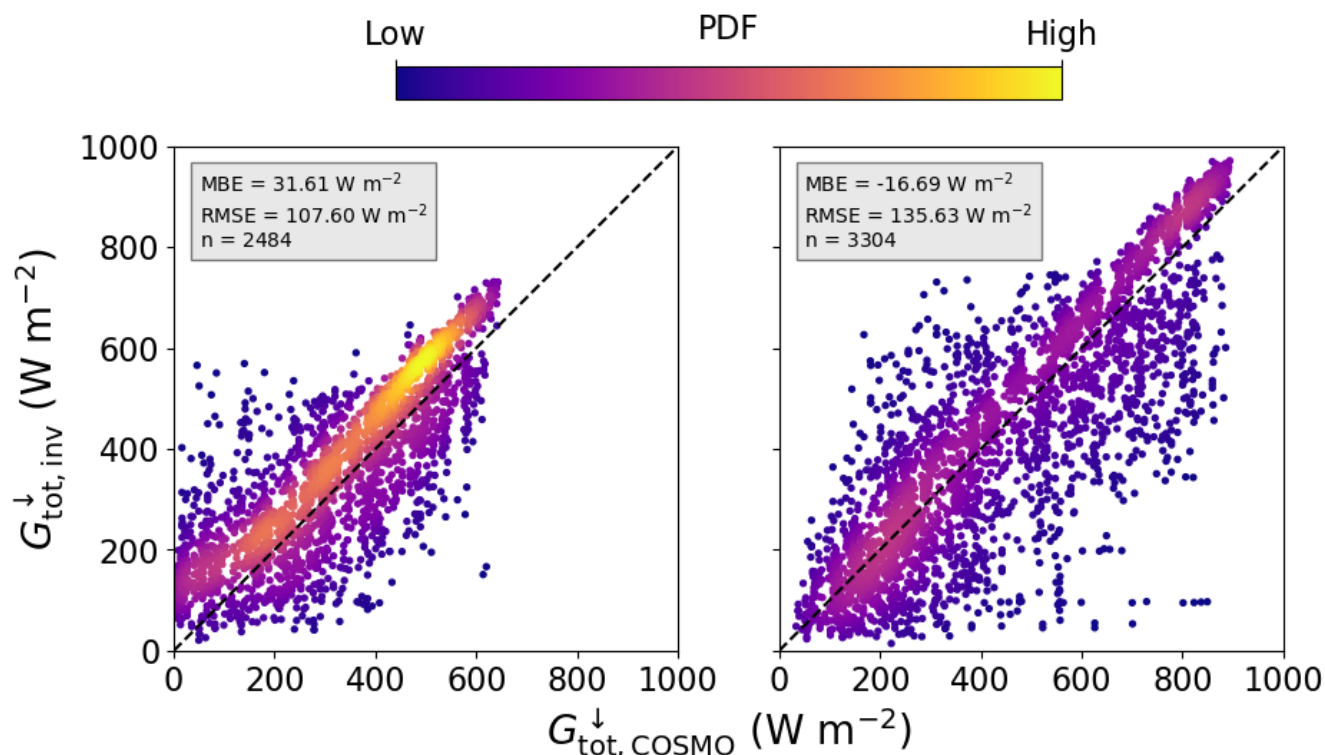


Figure 10. Combined comparison of GHI retrieved from 60 minute averaged PV power measurements under clear or completely cloudy conditions using the optical depth via DISORT LUT with that from the COSMO model, for all stations and for 2018 (left) and 2019 (right), using the linear temperature model.

4.4 Cloud optical depth retrievals

As discussed in Section 2.3.3, the cloud optical depth was retrieved from both PV systems and pyranometers, using a DISORT-based LUT. In order to avoid errors due to 3D effects, in this work only data with cloud fraction of 1 were considered, in other words only completely overcast conditions. The results for the linear temperature model are shown in Figs. 11 and 12, compared to the APOLLO_NG and COSMO data respectively. As can also be seen in Table 12, in most cases a smaller COD is extracted from PV systems, except for the comparison between the summer campaign and COSMO data, in which case a positive mean bias of approximately seven is found. Overall, the COD is mostly in the range between 1 and 10, for both campaigns.

Figures 13 and 14 show the same results using measured pyranometer data to infer the COD. These retrievals show the same trend as the PV-based ones: once again it is evident that the COD is mostly below 10, and in this range the retrieved data has a large positive relative bias. There are several possible reasons for this: firstly it is evident from Eq. (11) that the retrieval is more sensitive to errors in inverted irradiance (transmission) for smaller COD. In addition, since the LUT was constructed with



Table 12. Mean bias error and root mean squared error (in $W\ m^{-2}$) of COD retrievals from PV systems, compared to both APOLLO_NG data and COSMO model predictions.

Data	Measure	APOLLO_NG				COSMO			
		2018		2019		2018		2019	
		Linear	Faiman	Linear	Faiman	Linear	Faiman	Linear	Faiman
60min average	MBE	-2.51	-3.13	-2.68	-2.56	-8.31	-9.04	7.37	7.89
	RMSE	15.26	15.53	19.17	19.11	25.40	25.81	22.99	24.01

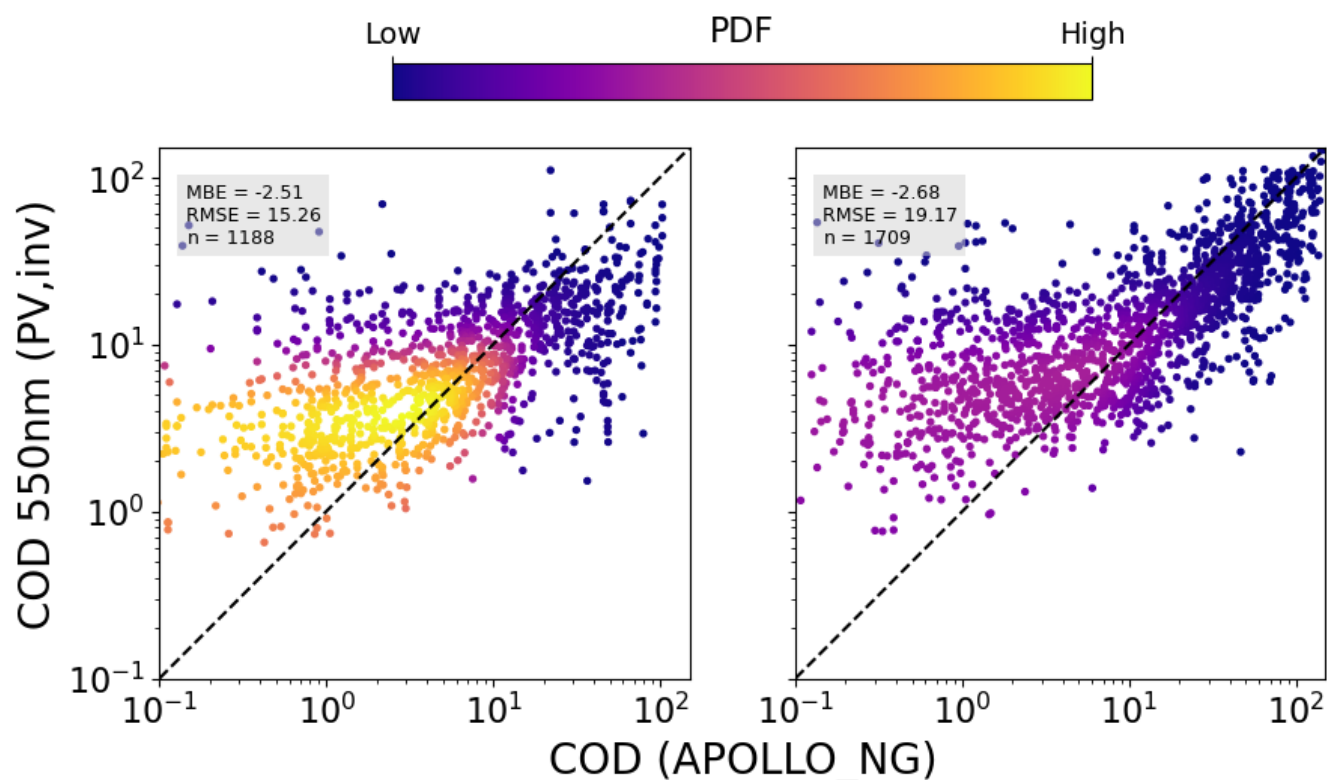


Figure 11. Combined comparison of COD retrieved from PV power measurements under completely cloudy conditions using the DISORT LUT with that from APOLLO_NG, for all stations and for 2018 (left) and 2019 (right), using the linear temperature model and averaged over 60 minutes.

water clouds, the effect of optically thinner ice clouds was not properly taken into account. Since ice particles scatter slightly less in the forward direction, $1 - g \simeq 0.3$ is larger than for water clouds ($1 - g \simeq 0.15$) and thus a smaller optical depth could lead to similar irradiance at the ground [cf. Eq. (11)]. Thirdly, since clouds become more absorbing in the near infrared and considering that silicon PV is sensitive to wavelengths up to 1200 nm, spectral effects could also lead to a bias in the results. In

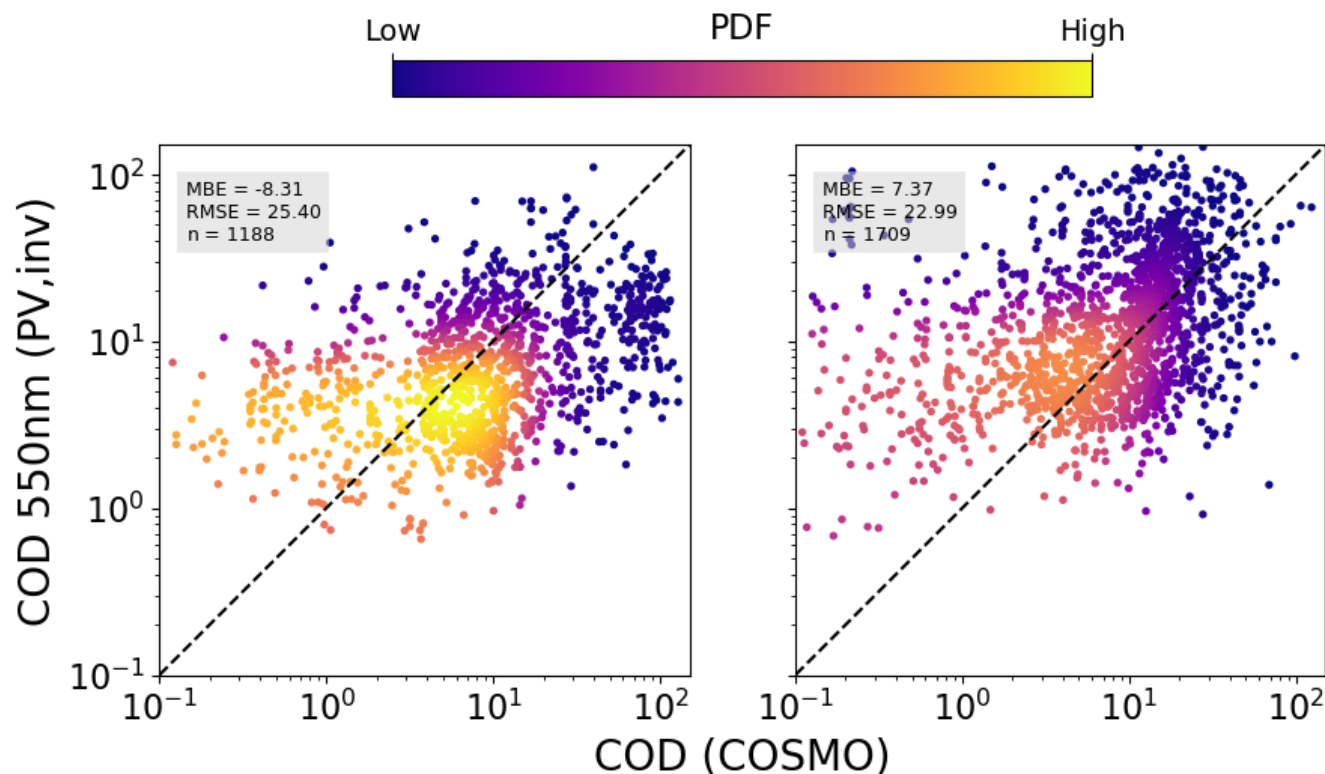


Figure 12. Same as 11, compared to the total COD from the COSMO model.

general it must be said that even with measurements at two different wavelengths there exists an ambiguity in the determination of effective radius and COD (Nakajima and King, 1990), so that in the case of spectrally integrated PV-inverted irradiance one cannot expect to have enough information to accurately determine cloud optical properties in all situations.

Notwithstanding the bias in COD retrievals, the ground-based method presented here can still complement satellite retrievals, in particular due to the potentially higher spatiotemporal resolution achievable with large amounts of high frequency data spread over a large area. Once again, for the summer months the COSMO data show a large mean bias error of 7.37, even for large values of COD, confirming the findings of Frank et al. (2018).

535 5 Conclusions and Outlook

In summary, in this work a framework for extracting both global tilted and horizontal irradiance from PV power data has been presented and a first test for retrieving cloud optical depth was carried out. The algorithm makes use of state-of-the-art radiative transfer solvers in libRadtran, in conjunction with different sources of data for the state of the atmosphere, in particular the aerosol and water vapour content. The calibration procedure uses an explicit calculation of diffuse and direct irradiance, taking

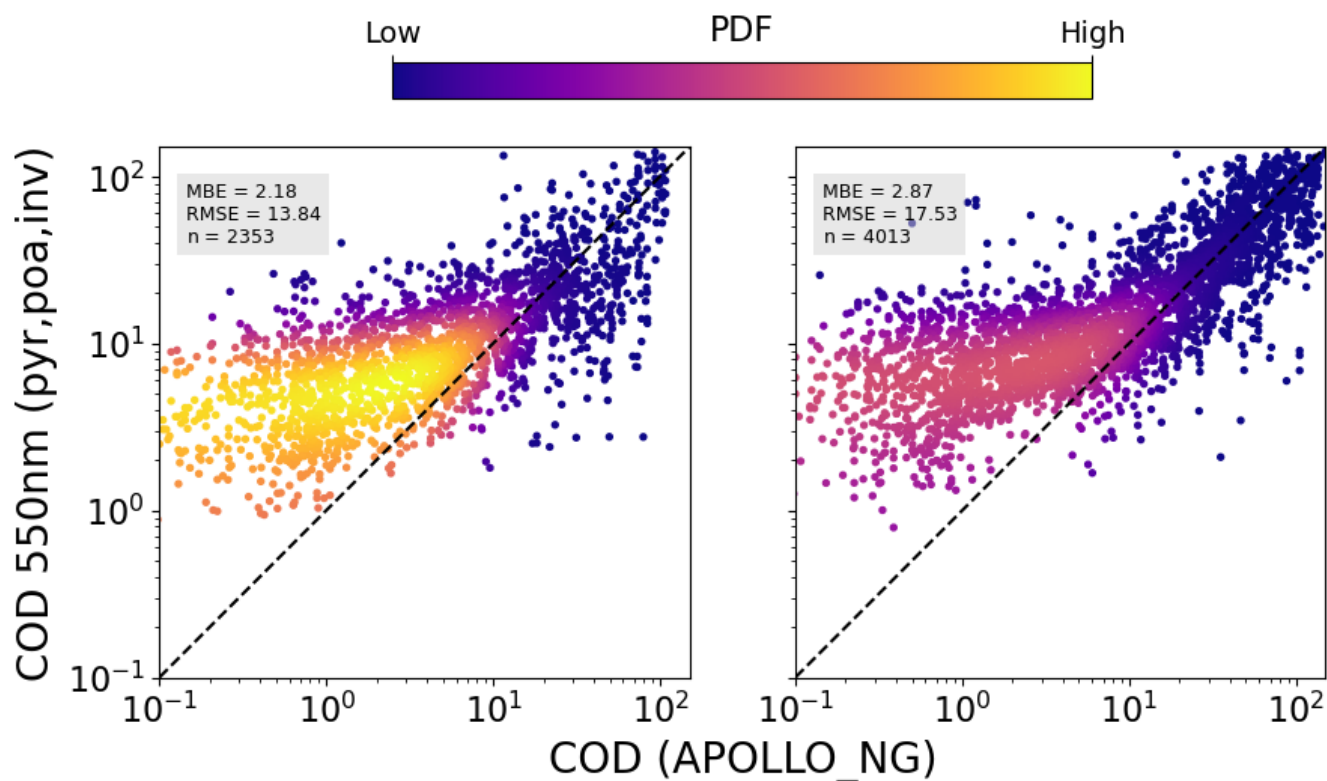


Figure 13. Combined comparison of COD retrieved from tilted (plane-of array = “poa”) pyranometer measurements under completely cloudy conditions using the DISORT LUT with that from APOLLO_NG, for all stations and for 2018 (left) and 2019 (right), using the linear temperature model and averaged over 60 minutes.

540 into account the spectral response of the relevant PV technology as well as the optical properties of the glass surface. Where
necessary the module temperature is modelled using weather model data for ambient temperature and wind speed input. The
PV systems are calibrated using a libRadtran clear sky simulation with the DISORT solver, with inputs from the COSMO
model and AERONET, and the algorithm can be adapted to each system and situation, depending on which parameters are
known and which need to be determined by non-linear optimisation.

545 Once calibrated, the measured PV data is used to extracted global tilted irradiance under all sky conditions. In order to
take into account the spectral mismatch between the spectral response of PV modules and the entire broadband spectrum, a
situation-dependent fit for the dependence of this mismatch on atmospheric conditions is performed, using simulated data for
clear sky conditions and the water vapour and aerosol load of each site. The GTI is then compared to that measured by tilted
pyranometers: the retrieved GTI at 1 minute (15 minute) resolution has a mean bias error of 19.69 W m^{-2} (23.25 W m^{-2})
550 averaged over the two measurement campaigns, using the linear temperature model. The non-linear Faiman temperature model
achieves a mean bias error of 10.41 W m^{-2} for those systems with 1 minute data, but for those with 15 minute the calibration

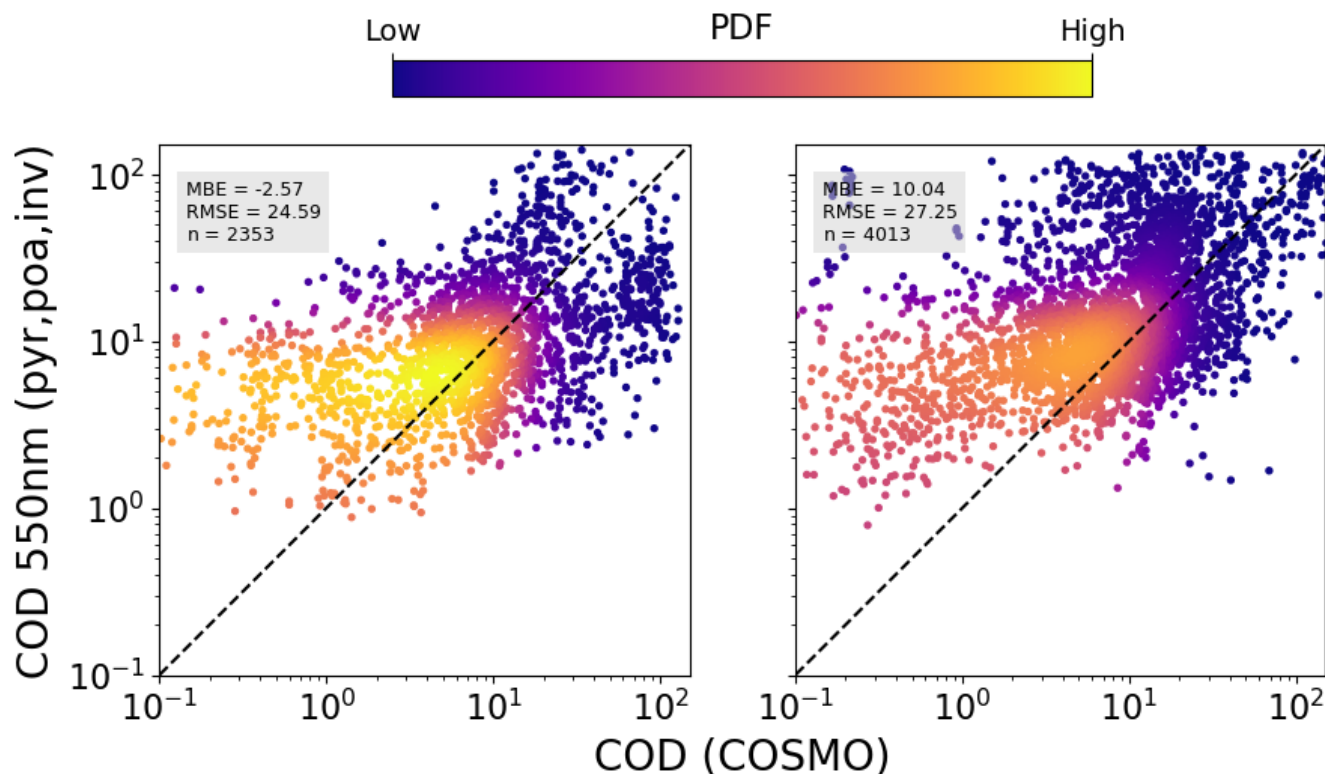


Figure 14. Same as 13, compared to the total COD from the COSMO model.

algorithm fails to find an optimal solution in several cases, so that in the end the mean bias error is 87.17 W m^{-2} . This shows that an accurate calibration is essential in order to accurately extract irradiance.

The inverted GTI is used to find the global horizontal irradiance using two different methods: (i) under persisting clear or
555 cloudy conditions (either completely clear or completely cloudy skies) a lookup table based on a 1D DISORT simulation is
used in order to find either the AOD or COD, and thus the global horizontal irradiance; (ii) under broken cloud conditions a
LUT based on 3D MYSTIC simulations is used to translate the tilted to horizontal irradiance, using the geometry of the system,
sun position and cloud fraction as inputs. The retrieved GHI is then compared to pyranometer measurements: in the case of
the 1D LUT method and with 1 minute data und clear or completely cloudy skies, the mean bias error is 11.45 W m^{-2} for the
560 linear model and 5.36 W m^{-2} for the non-linear model. Comparison with CAMS data reveals a negative bias: the 60 minute
data shows a bias of -10.69 W m^{-2} in autumn (mostly clear skies) and -46.30 W m^{-2} in summer (mostly cloudy skies), for the
linear temperature model. As discussed in Section 1, this confirms the results in Yang and Bright (2020), who showed that both
CAMS and SARA H tend to slightly overestimate GHI. However, considering that the inferred GHI has a positive bias with
respect to pyranometers, these results must be interpreted with care. In the case of clear skies, small errors in the temperature



565 model can lead to large errors in extracted irradiance, and the case of cloudy skies, simplifying assumptions on cloud type can lead to errors in COD and extracted irradiance.

The retrieved GHI shows a large bias when comparing it with COSMO model data, thus confirming the results of Frank et al. (2018); Zubler et al. (2011): in autumn the 60 minute averaged GHI has a mean bias error of 31.61 W m^{-2} , since COSMO has in general a too large aerosol load, whereas in summer the MBE is -16.69 W m^{-2} , since under cloudy conditions the COSMO
570 model overestimates the irradiance. The latter result is also confirmed by the COD retrievals: in summer there is a positive bias of 7.37 for the retrieved COD relative to COSMO – the COD in the weather model is thus on average too small.

Overall, the largest source of error in the model chain comes from the PV model itself – an accurate calibration is vital in order to be able to extract irradiance reliably. In this regard it is helpful to use measured module temperature rather than relying on temperature models. More accurate results could be achieved by using PV current measurements, since in this case
575 the temperature dependence is almost negligible. This will be explored in future work.

The DISORT LUT was only employed during periods of persistent cloudy or clear sky conditions in order to infer COD or AOD, respectively, whereas the effect of 3D transport of photons was only taken into account with the MYSTIC LUT for the GHI. This means that the algorithm in its present form can only extract direct and diffuse components reliably under stable conditions for which 1D radiative transfer is still a reasonable approximation. A possible extension to this will be studied in
580 future work, in which explicit 3D simulated cloud fields will be used in conjunction with the 1D DISORT simulation in order to quantify the error that results from neglecting 3D radiative transfer. It is only once the three dimensionality of atmospheric radiative transfer as well as additional information on cloud type is taken into account that one can accurately extract the direct and diffuse irradiance components under broken cloud conditions.

Another aspect not taken into account in this study is the possible gain in using several different PV systems that are close
585 enough to each other so as to be able to see the same or similar portions of the sky. In this case it is conceivable that one could extract more information about cloud properties and irradiance compared to that obtained from just one system. Indeed, the rapid proliferation of PV installations could make such multi-sensor inversions an interesting future prospect.

The ultimate goal of this work is to show that PV power data can be used to infer global horizontal irradiance and optical properties of the atmosphere. If this could be achieved at a large scale it would allow a better characterisation of solar irradiance
590 at the ground and open up several possibilities for improving PV power forecasts at different time horizons. At shorter time (sub-hourly) scales one could use the additional information on irradiance variability as further input to empirical forecasts based on statistical methods, whereas at longer time scales (more than three hours) these data could be assimilated into weather models. In order for this to make a difference one needs a much larger data set of PV systems for the analysis. This in itself will require more of the algorithm to be automated, in particular the pre-processing of the data, removing unwanted artefacts,
595 clear sky detection, as well as the separation of data into different weather conditions. First steps in this direction are currently being explored.

Code and data availability. Data and code is available for download as part of the supplementary information.



Appendix A: Modelling details

A1 Parametric power model

600 In Buchmann (2018) a simple model was proposed, based on the combination of several different modelling steps from the literature (see for instance Skoplaki and Palyvos (2009) or Dows and Gough (1995)). Here the PV power output is written as

$$P_{AC,mod} = A \eta_{DCAC} \eta_{module}(T, G_{tot,SW,\tau}^{\angle}, v_{wind}) G_{tot,PV,\tau}^{\angle} = A \eta_{DCAC} \eta_{module}(T, G_{tot,SW,\tau}^{\angle}, v_{wind}) [G_{dir,PV,\tau}^{\angle} + G_{diff,PV,\tau}^{\angle}], \quad (A1)$$

where A is the surface area of the PV system, η_{DCAC} is the converter efficiency, and the direct and diffuse components of the irradiance in the plane-of-array and underneath the glass covering (see Sect. A2) are given by $G_{dir,PV,\tau}^{\angle}$ and $G_{diff,PV,\tau}^{\angle}$ respectively. The temperature-dependent module efficiency is defined by (Evans and Florschuetz, 1977)

$$\eta_{module}(T, G_{tot,SW,\tau}^{\angle}, v_{wind}) = \eta_{module,n} [1 - \zeta(T_{module} - T_n)], \quad (A2)$$

where $\eta_{module,n}$ and ζ are the module efficiency and temperature coefficient at STC, i.e. at $T_n = 25^{\circ}\text{C}$, $G_{tot,SW,n}^{\angle} = 1000 \text{ W m}^{-2}$ and air-mass of 1.5. The module temperature is modelled using both the linear model (TamizhMani et al., 2003) defined by

$$T_{module} = u_0 T_{ambient} + u_1 G_{tot,SW,\tau}^{\angle} + u_2 v_{wind} + u_3 T_{sky}, \quad (A3)$$

610 as well as the non-linear model (Barry et al., 2020; Faiman, 2008) defined by

$$T_{module} = T_{ambient} + \frac{G_{tot,SW,\tau}^{\angle}}{u_1 + u_2 v_{wind}} + u_3 (T_{sky} - T_{ambient}), \quad (A4)$$

where v_{wind} is the wind speed at 10m above the ground, $T_{sky}^4 = G_{LW}^{\downarrow} / (\epsilon \sigma)$ defines the sky temperature and $u_{0,1,2,3}$ are model parameters. Here an emissivity of $\epsilon = 1$ is assumed and σ is the Stefan-Boltzmann constant. Note that Eqs. (A1), (A2) and (A3) ((A4)) can be combined into the general non-linear expressions given in Eq. (1) (Eq. (2)) (see for instance Skoplaki and Palyvos (2009); Dows and Gough (1995)), where in this special case the coefficients are given by

$$b_1 = s(1 + \zeta 25), \quad b_2 = -u_1 s \zeta, \quad b_3 = -u_0 s \zeta, \quad b_4 = -u_2 s \zeta, \quad b_5 = -s \zeta u_3 \quad (A5)$$

for the linear and

$$b'_1 = s(1 + \zeta 25), \quad b'_2 = -\frac{u_1}{s \zeta}, \quad b'_3 = s \zeta (u_3 - 1), \quad b'_4 = -\frac{u_2}{s \zeta}, \quad b'_5 = -s \zeta u_3. \quad (A6)$$

for the non-linear temperature model, where $s \equiv A \eta_{DCAC} \eta_{module,STC}$ is a constant scaling factor. The model equations in Eqs. (1) and (2) are used in this work, and the coefficients $u_{0,1,2,3}$, ζ , s are allowed to vary freely, unless their a priori values are known from datasheets and/or from temperature modelling. In cases where measured temperature is available the parameters $u_{0,1,2,3}$ fall away.



A2 Optical model of glass covering

A2.1 Model formulation

625 In order to model the optics of the glass surface of the PV modules the following equation for the transmission of photons as a function of the incident angle Θ is used (De Soto et al., 2006; Sjerps-Koomen et al., 1996)

$$\tau_{\text{PV}}(\Theta) = \exp\left(-\frac{\kappa L}{\cos\Theta_r}\right) \left(1 - \frac{1}{2} \left[\frac{\sin^2(\Theta_r - \Theta)}{\sin^2(\Theta_r + \Theta)} + \frac{\tan^2(\Theta_r - \Theta)}{\tan^2(\Theta_r + \Theta)}\right]\right), \quad (\text{A7})$$

where Θ_r is the angle of refraction from Snell's law ($n \sin\Theta_r = \sin\Theta$), n is the index of refraction of glass, κ is the glazing extinction coefficient and L is the glazing thickness. The incident angle Θ is the angle between the solar position vector and
 630 normal vector of the PV array, defined by

$$\cos\Theta = \cos\theta_0 \cos\theta + \sin\theta_0 \sin\theta \cos(\phi_0 - \phi), \quad (\text{A8})$$

where θ is the angle of inclination of the PV array, ϕ is its orientation, θ_0 is the solar zenith angle and ϕ_0 is the solar azimuth.

In principle one should take into account the wavelength dependence of n and κ , however for most materials they are relatively constant, with n increasing slightly at lower wavelengths, and since in practice the exact properties of the glass
 635 covering for each system are unknown it suffices to use the effective values for all wavelengths.

The so-called incidence angle modifier (see also Duffie and Beckman (2013)) is defined by the ratio of the transmission $\tau_{\text{PV}}(\Theta)$ and the transmission at normal incidence, i.e.,

$$\tau_{\text{PV,rel}}(\Theta) \equiv \frac{\tau_{\text{PV}}(\Theta)}{\tau_{\text{PV}}(0)}, \quad (\text{A9})$$

where

$$640 \quad \tau_{\text{PV}}(0) = e^{-\kappa L} \left[1 - \left(\frac{n-1}{n+1}\right)^2\right] \quad (\text{A10})$$

$$= e^{-\kappa L} \frac{4n}{(n+1)^2}. \quad (\text{A11})$$

The use of a relative transmission coefficient is justified from the fact that the absolute transmittance is already taken into account when characterising the solar cell under standard conditions (Sjerps-Koomen et al., 1996). The normalisation with $\tau_{\text{PV}}(0)$ means that the result is less sensitive to the product κL and more on the angle of incidence. In the forward model the
 645 wavelength-integrated direct irradiance as well as the diffuse radiance beams are each multiplied with the factor $\tau_{\text{PV,rel}}(\Theta)$ in order to take into account the attenuation due to the glass surface. The values of the extinction coefficient and thickness of the glass were fixed to (De Soto et al., 2006) $\kappa = 4 \text{ m}^{-1}$ and $L = 0.002 \text{ m}$, respectively, whereas the effective refractive index n was allowed to vary ($n = 1.526$ with an a-priori error of 1%). In principle one could also vary the product κL that controls the absorption, but as mentioned above the incident angle modifier approach is applicable for a wide range of glass covers (Duffie
 650 and Beckman, 2013; Klein, 1979).



A2.2 Optical model in forward model calibration

In the forward model calibration, the transmission function can then be used to calculate the direct and diffuse irradiance, $G_{\text{dir,PV},\tau}^{\angle}$ and $G_{\text{diff,PV},\tau}^{\angle}$ as

$$G_{\text{dir,PV},\tau}^{\angle} = \frac{\cos \Theta}{\cos \theta_0} G_{\text{dir}}^{\downarrow} \tau_{\text{PV,rel}}(\Theta), \quad (\text{A12})$$

655 and

$$G_{\text{diff,PV},\tau}^{\angle} = \int_{\phi}^{2\pi+\phi} \int_{-\theta}^{\pi/2-\theta} L_{\text{diff}}^{\Omega} \cos \Theta' \tau_{\text{PV,rel}}(\Theta') d\Omega, \quad \text{for } \cos \Theta' \geq 0, \quad (\text{A13})$$

where L_{diff}^{Ω} is the diffuse radiance distribution calculated by DISORT. In this way there is no need for an empirical incidence angle modifier, since the direction of each diffuse photon is explicitly described. The same formulation was used to calculate $G_{\text{dir,SW},\tau}^{\angle}$ and $G_{\text{diff,SW},\tau}^{\angle}$, i.e. over the whole wavelength range.

660 A2.3 Inversion of the optical model

For the inversion of the PV model, two different methods were used: for the extraction of cloud optical depth with DISORT the optical model can be explicitly taken into account in the radiative transfer simulation, whereas for the direct extraction of GTI and its translation to GHI with the MYSTIC lookup table the empirical formulation (Duffie and Beckman, 2013) for the effective angle for diffuse photons as a function of tilt angle θ ,

$$665 \quad \Theta_{\text{diff}} = 59.7 - 0.1388\theta + 0.001497\theta^2 \quad (\text{A14})$$

was used for all time points with clearness index below 0.3, so that the final inverted GTI is given by

$$G_{\text{tot,SW,inv}}^{\angle} = \frac{G_{\text{tot,SW,inv},\tau}^{\angle}}{\tau_{\text{PV,rel,eff}}}, \quad (\text{A15})$$

where

$$\tau_{\text{PV,rel,eff}} = \begin{cases} \tau_{\text{PV,rel}}(\Theta_{\text{dir}}) & \text{if } k_i \geq 0.3 \\ \tau_{\text{PV,rel}}(\Theta_{\text{diff}}) & \text{if } k_i < 0.3 \end{cases} \quad (\text{A16})$$

670 is the effective incidence angle modifier for clearness index k_i .

A3 Spectral mismatch fitting procedure

The ratio of silicon PV irradiance to broadband irradiance as defined in Eq. (5) is a function of atmospheric composition (primarily water vapour content) and angle of incidence of the incoming solar beam. Indeed, the shape of the diurnal variation in $\xi_{\text{spec,GTI}}$ is dependent on the azimuth angle of the PV plant, as shown in Figs. A1 and A2, where the ratio is plotted for

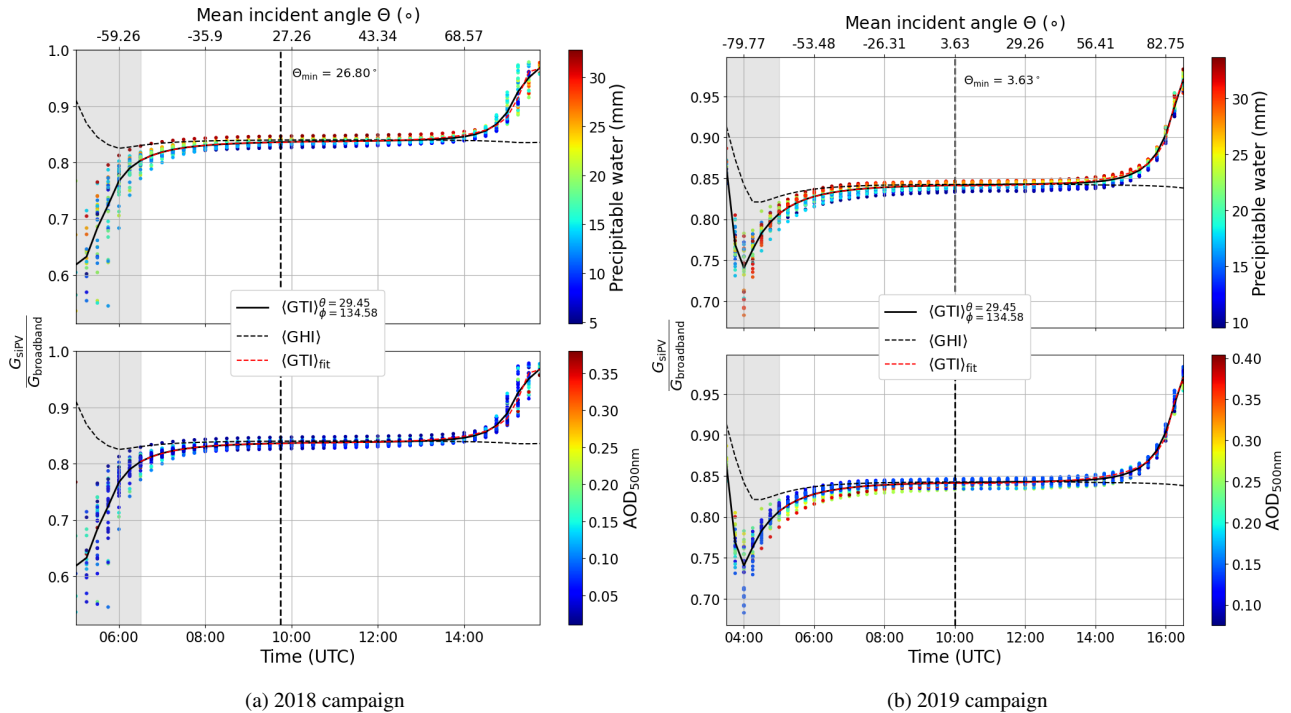


Figure A1. Spectral mismatch ratio at PV12 (azimuth angle $\phi \simeq 135^\circ$) as a function of time, mean incident angle as well as water vapour column (upper plots) and AOD (lower plots), both (a) 2018 and (b) 2019 measurement campaigns. Θ_{min} is the minimum incident angle.

675 both GHI and GTI, for two different PV systems with different orientation, using libRadtran clear sky simulations from the different measurement campaigns. The points in the upper (lower) plots in each figure are coloured according to precipitable water (AOD), and it is evident that for a given incident angle the water vapour plays the largest role in determining the ratio.

The mismatch ratio remains at roughly 0.83 throughout the day, depending on water vapour column. In the case of PV12 in Fig. A1, one can see that in the mornings the ratio is smaller, i.e. more red light, whereas in the evenings the ratio is larger, since the panel is facing more to the south east. This means that the panel detects more diffuse light in the evenings. The behaviour at PV15 (Fig. A1) is the opposite – in the morning the ratio is larger, since the panel looks more to the south west (mornings higher diffuse component, i.e. more blue light), whereas in the evenings it is smaller. However in the summer time when the sun goes down far to the north, the diffuse component again plays a role, so that the ratio becomes larger (right hand plot).

As shown in the Figures above, the data was first grouped by time of day in order to calculate the mean value, then split into two halves on either side of the minimum incident angle (Θ_{min}). Each branch can then be fitted with the function

$$\langle \xi_{\text{spec,GTI}} \rangle = x_0 \exp \left(-\frac{x_1}{\cos \Theta} - \frac{x_2}{\cos^2 \Theta} \right), \quad (\text{A17})$$

shown as the red dashed line in Figs. A1 and A2. This shows the general form of the diurnal variation in spectral mismatch, and that for silicon PV the ratio is about 83% for most of the day.

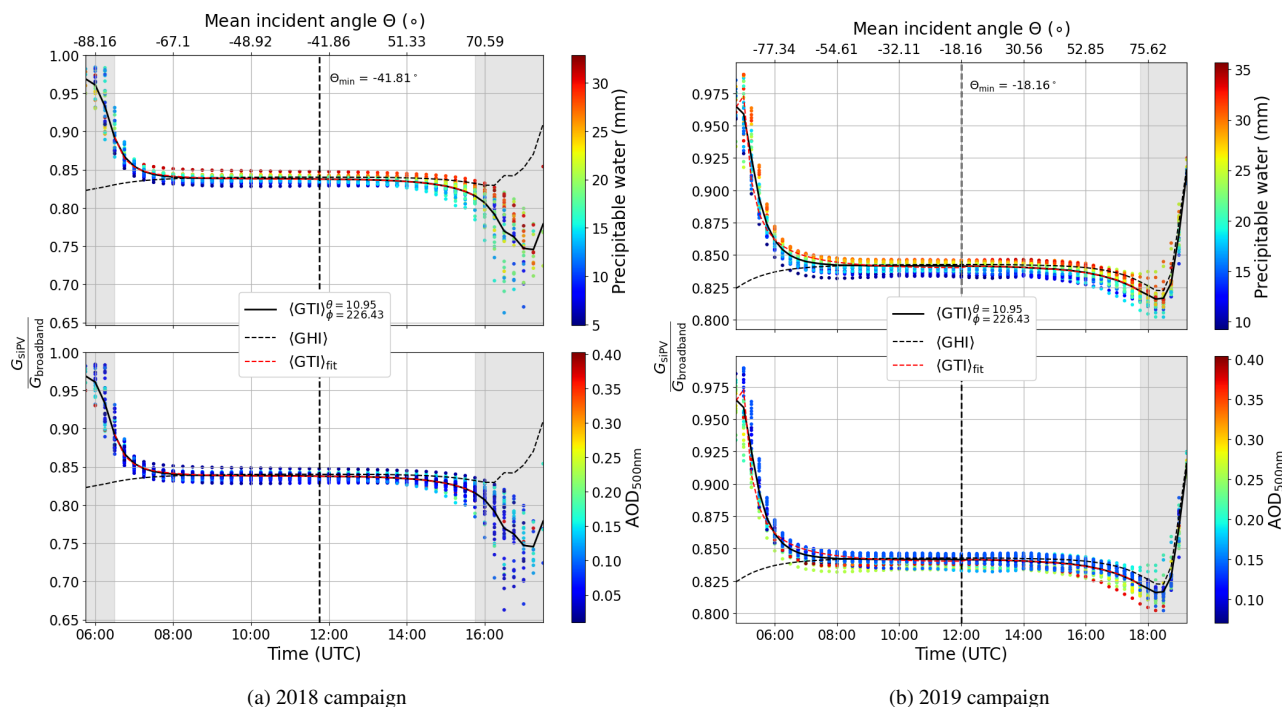


Figure A2. Same as A1, for PV15 (azimuth angle $\phi \simeq 226^\circ$)

In order to capture the effect of precipitable water and AOD, the function

$$\xi_{\text{spec,GTI}} = p_0 \exp(-p_1 w - p_2 a) \quad (\text{A18})$$

is fitted to the irradiance data for each time step (averaged over all days of the respective measurement campaign), where w is the precipitable water from COSMO and a the AOD at 500nm from AERONET. The fit coefficients are then interpolated over the entire dataset in order to calculate $\xi_{\text{spec,GTI}}$ at any time of day. Future work will examine the effects of clouds on the spectral mismatch factor – here the clear sky fit was applied to all data, which due to whitening of the skylight by clouds could lead to a bias in the final result.

Appendix B: Results using Faiman temperature model

In this section more retrieval plots using the Faiman temperature model are shown for completeness, for GTI (Figs. B1 and B2) and GHI (Figs. B3, B4 and B5). The corresponding statistical quantities are shown in the main text, together with those from the linear temperature model in Tables 10, 11 and 12.

Here the result of errors in the calibration procedure using 15 minute data with the Faiman model can be clearly seen. For instance if there is a large correlation between temperature model parameters and orientation angles, the optimisation may find a local minimum with an incorrect azimuth angle, leading to incorrect results for the irradiance. If the algorithm cannot find a

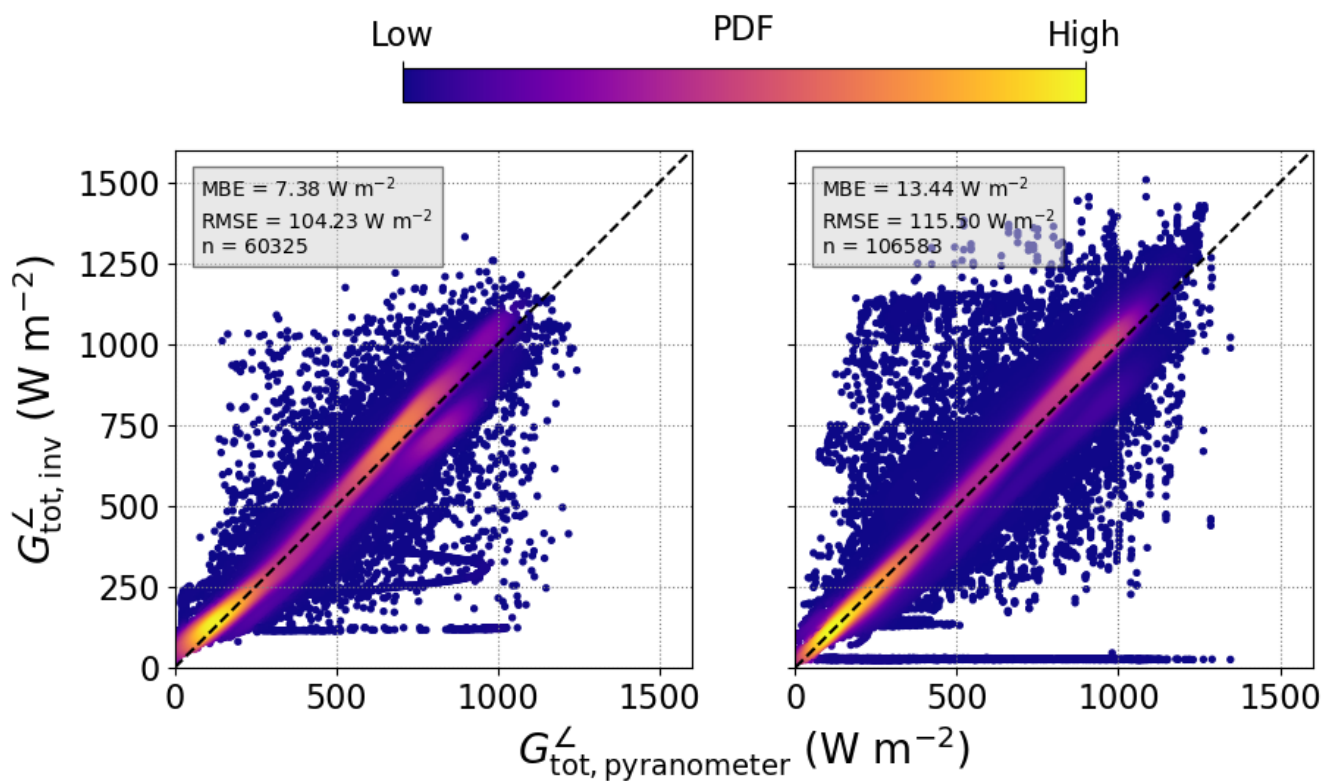


Figure B1. Combined comparison of GTI retrieved from PV power measurements with that measured by tilted pyranometers, using data in 1 minute resolution from MS02, PV11, PV12, PV15, PV19, for 2018 (left) and 2019 (right), and the Faiman temperature model.

satisfactory solution then the a-priori values are used, which then leads to a large error in the extracted tilted irradiance as seen in Fig. B2.

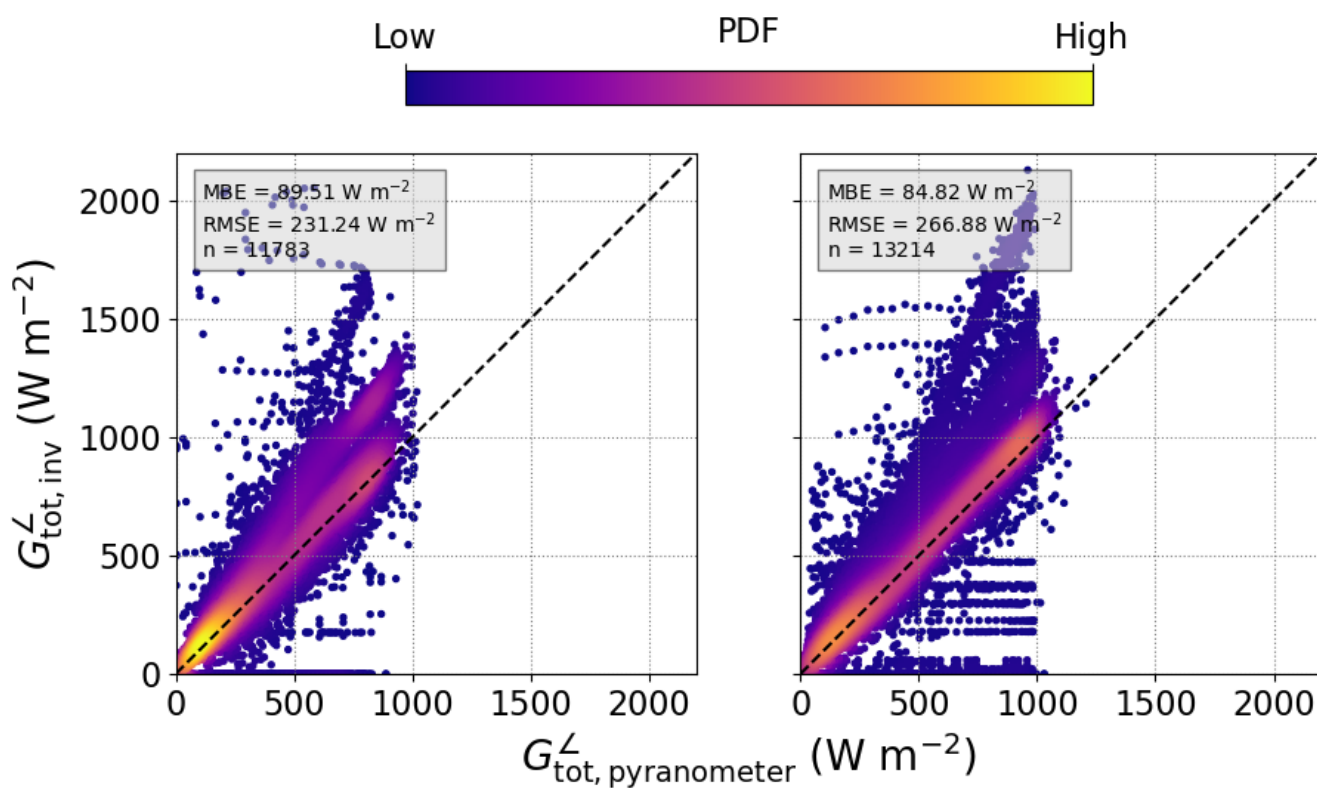


Figure B2. Same as Fig. B1 using data in 15 minute resolution from MS02, PV01, PV06, PV08, PV10, PV11, PV14, PV16, PV17, PV18, PV21 for 2018 (left) and 2019 (right).

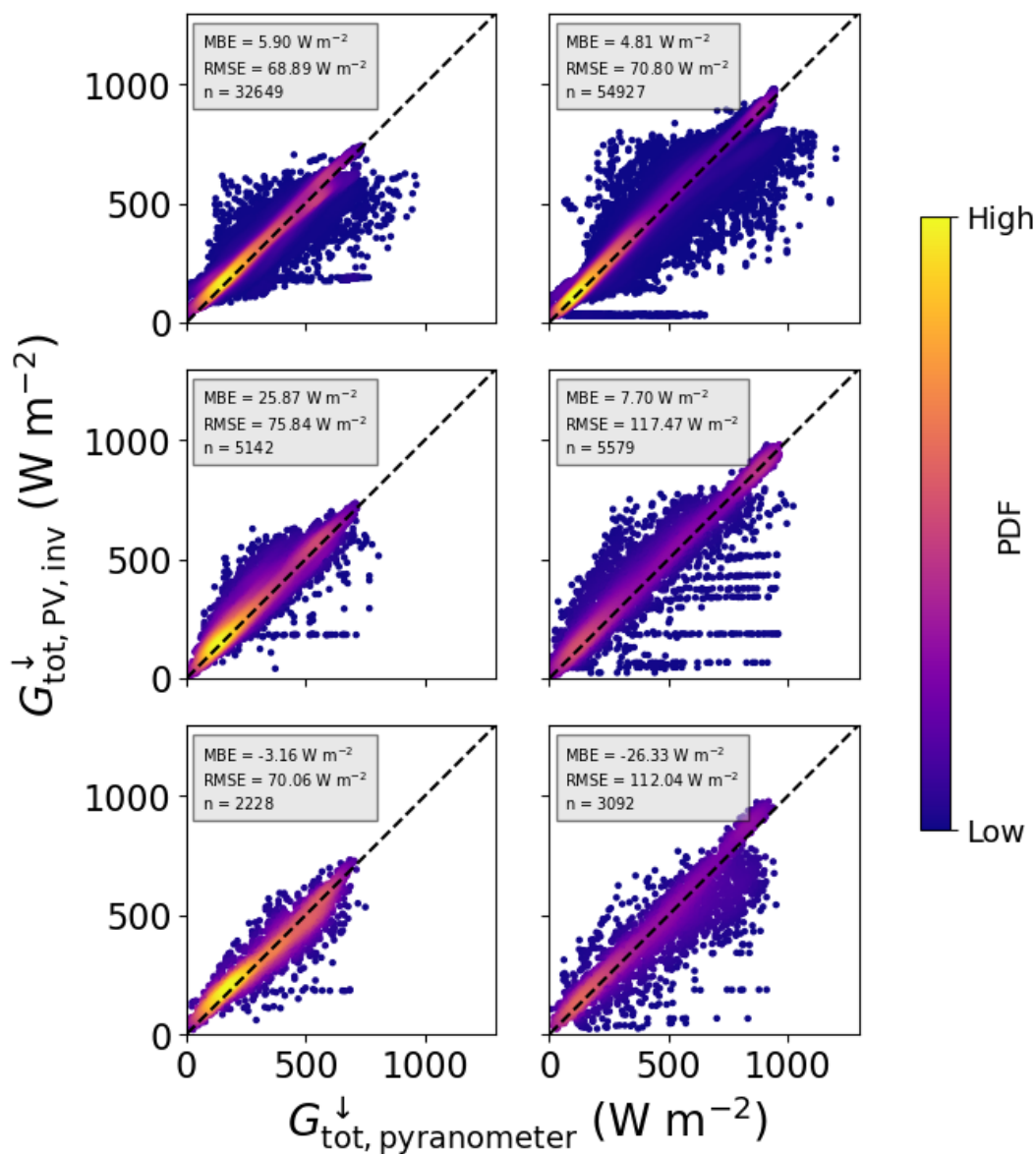


Figure B3. GHI from DISORT LUT compared to horizontal pyranometers, as in 7, for the Faiman temperature model.

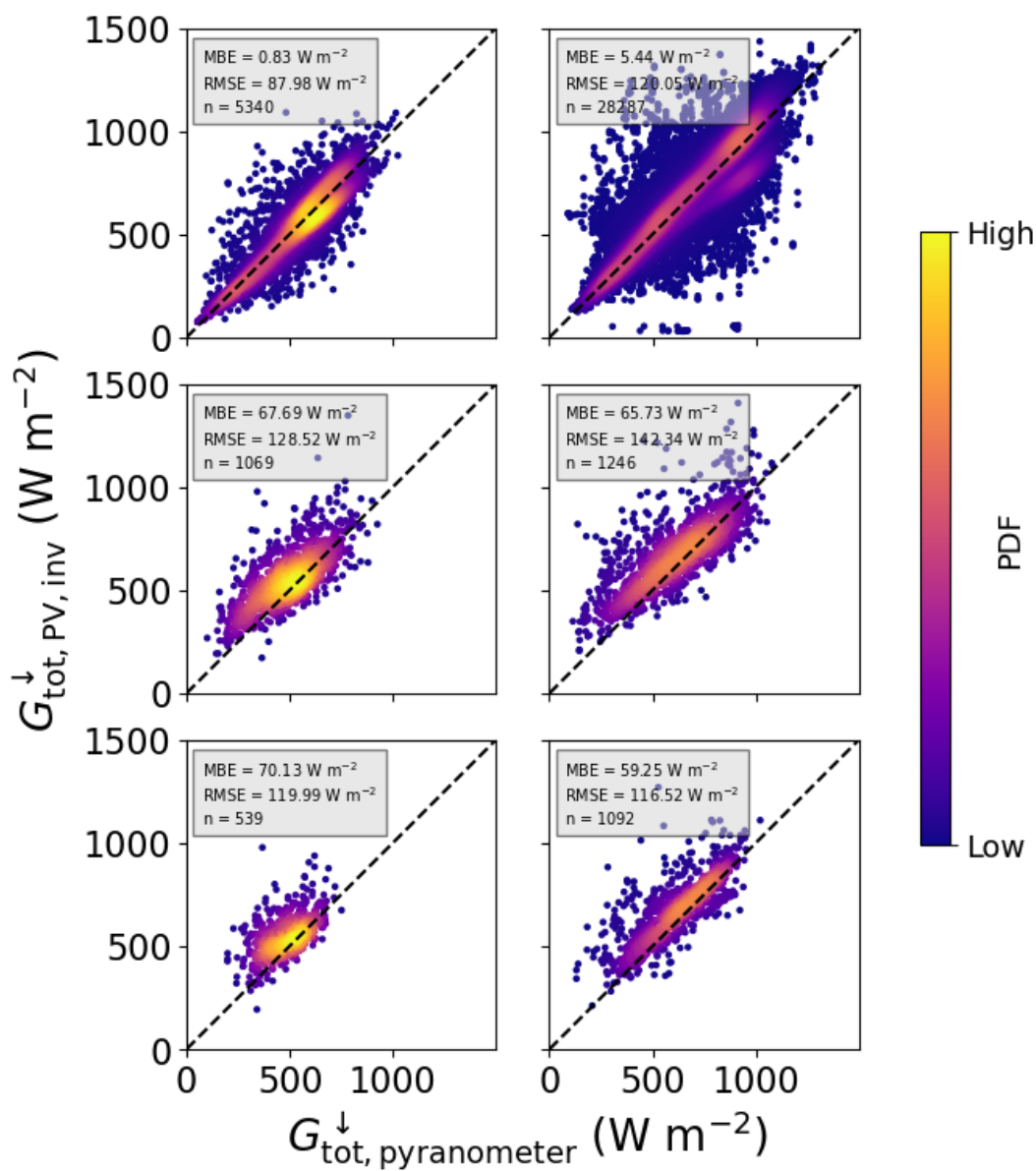


Figure B4. GHI from MYSTIC LUT compared to horizontal pyranometers, as in 8, for the Faiman temperature model.

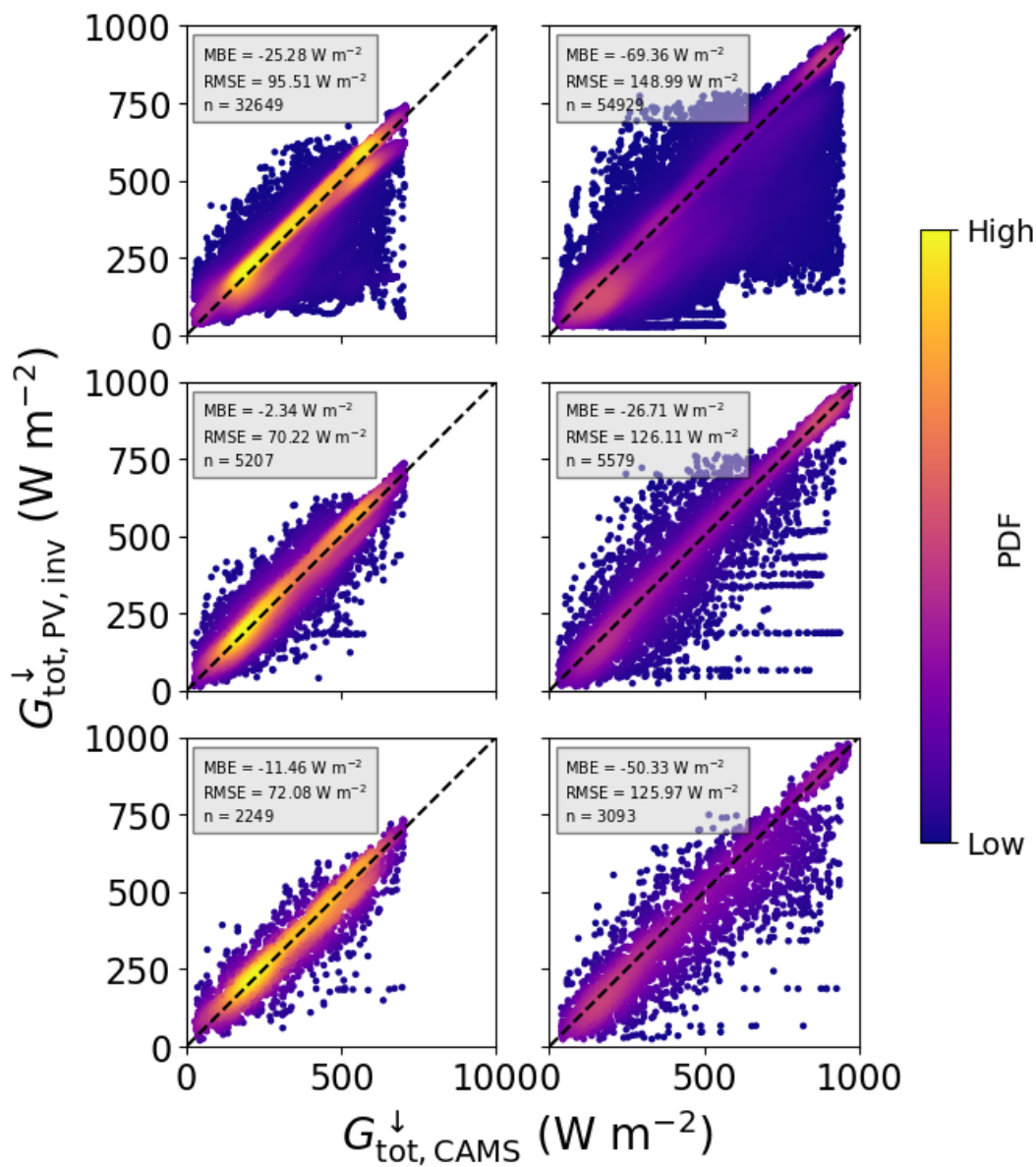


Figure B5. GHI using DISORT LUT compared to satellite measurements, as in 9, for the Faiman temperature model.



705 *Author contributions.* The two measurement campaigns were designed and coordinated with contributions from all authors, and the instal-
lation and calibration of the various measurement devices was performed by NK, CS, RY, HD, JW, FG, PH and MS. The PV model was
conceptualised by JB, TB, KP, AH-C and SM; the software and simulations to implement and validate the model were developed and carried
out by JB, with contributions from JG, FG and AH-C. FG wrote several Python subroutines in order to import weather model data and
also developed the MYSTIC lookup table. CE and BM introduced several customised features into libRadtran for this work; LS and MS-H
710 provided weather model and satellite data. JB prepared the manuscript with contributions from all co-authors.

Competing interests. One author (BM) is a member of the editorial board of AMT. The peer-review process was guided by an independent
editor, and the authors have also no other competing interests to declare.

Acknowledgements. The authors acknowledge support from the German Federal Ministry for Economic Affairs and Energy (BMWi) under
the project “MetPVNet: Entwicklung innovativer satellitengestützter Methoden zur verbesserten PV-Ertragsvorhersage auf verschiedenen
715 Zeitskalen für Anwendungen auf Verteilnetzebene”, with project code 0350009. The DWD is thanked for the provision of COSMO model
data. JB would like to thank Lukas Tirpitz for helpful comments and suggestions in the development of this work.



References

- 720 Abe, C. F., Dias, J. B., Notton, G., and Poggi, P.: Computing Solar Irradiance and Average Temperature of Photovoltaic Modules from the Maximum Power Point Coordinates, *IEEE Journal of Photovoltaics*, 10, 655–663, <https://doi.org/10.1109/JPHOTOV.2020.2966362>, 2020.
- Alonso-Abella, M., Chenlo, F., Nofuentes, G., and Torres-Ramírez, M.: Analysis of spectral effects on the energy yield of different PV (photovoltaic) technologies: The case of four specific sites, *Energy*, 67, 435–443, <https://doi.org/https://doi.org/10.1016/j.energy.2014.01.024>, 2014.
- 725 Baldauf, M., Seifert, A., Förstner, J., Majewski, D., Raschendorfer, M., and Reinhardt, T.: Operational Convective-Scale Numerical Weather Prediction with the COSMO Model: Description and Sensitivities, *Monthly Weather Review*, 139, 3887–3905, <https://doi.org/10.1175/MWR-D-10-05013.1>, 2011.
- Barry, J., Böttcher, D., Pfeilsticker, K., Herman-Czezuch, A., Kimiaie, N., Meilinger, S., Schirrmeister, C., Deneke, H., Witthuhn, J., and Göttsche, F.: Dynamic model of photovoltaic module temperature as a function of atmospheric conditions, *Adv. Sci. Res.*, 17, 165–173, <https://doi.org/10.5194/asr-17-165-2020>, 2020.
- 730 Boers, R.: Simultaneous retrievals of cloud optical depth and droplet concentration from solar irradiance and microwave liquid water path, *Journal of Geophysical Research: Atmospheres*, 102, 29 881–29 891, <https://doi.org/https://doi.org/10.1029/97JD02494>, 1997.
- Boers, R., van Lammeren, A., and Feijt, A.: Accuracy of Cloud Optical Depth Retrievals from Ground-Based Pyranometers, *Journal of Atmospheric and Oceanic Technology*, 17, 916–927, [https://doi.org/10.1175/1520-0426\(2000\)017<0916:AOCODR>2.0.CO;2](https://doi.org/10.1175/1520-0426(2000)017<0916:AOCODR>2.0.CO;2), 1999.
- Buchmann, T.: Potenzial von Photovoltaikanlagen zur Ableitung raum-zeitlich hoch aufgelöster Globalstrahlungsdaten, Phd thesis, Heidelberg University, <https://doi.org/10.11588/heidok.00024687>, 2018.
- Bundesverband Solarwirtschaft e.V.: Statistische Zahlen der deutschen Solarstrombranche (Photovoltaik), Tech. rep., Berlin, <https://www.solarwirtschaft.de/datawall/uploads/2022/02/bsw{ }faktenblatt{ }photovoltaik.pdf>, 2021.
- Buras, R., Dowling, T., and Emde, C.: New secondary-scattering correction in DISORT with increased efficiency for forward scattering, *Journal of Quantitative Spectroscopy and Radiative Transfer*, 112, 2028–2034, <https://doi.org/https://doi.org/10.1016/j.jqsrt.2011.03.019>, 740 2011.
- Carrasco, M., Mancilla-David, F., and Ortega, R.: An Estimator of Solar Irradiance in Photovoltaic Arrays With Guaranteed Stability Properties, *IEEE Transactions on Industrial Electronics*, 61, 3359–3366, <https://doi.org/10.1109/TIE.2013.2281154>, 2014.
- Črnivec, N. and Mayer, B.: Quantifying the bias of radiative heating rates in numerical weather prediction models for shallow cumulus clouds, *Atmospheric Chemistry and Physics*, 19, 8083–8100, <https://doi.org/10.5194/acp-19-8083-2019>, 2019.
- 745 De Soto, W., Klein, S. A., and Beckman, W. A.: Improvement and validation of a model for photovoltaic array performance, *Solar Energy*, 80, 78–88, <https://doi.org/10.1016/j.solener.2005.06.010>, 2006.
- Deneke, H.: Influence of clouds on the solar radiation budget, Phd thesis, Rheinische Friedrich-Wilhelms-Universität Bonn, <http://bibliothek.knmi.nl/knmipubWR/WR2002-09.pdf>, 2002.
- Dows, R. N. and Gough, E. J.: PVUSA model technical specification for a turnkey photovoltaic power system, Tech. rep., Department of Energy, <https://doi.org/10.2172/172103>, 1995.
- 750 Duffie, J. A. and Beckman, W. A.: Radiation Transmission through Glazing: Absorbed Radiation, chap. 5, pp. 202–235, John Wiley & Sons, Ltd, <https://doi.org/10.1002/9781118671603.ch5>, 2013.



- Elsinga, B., van Sark, W., and Ramaekers, L.: Inverse photovoltaic yield model for global horizontal irradiance reconstruction, *Energy Science and Engineering*, 5, 226–239, <https://doi.org/10.1002/ese3.162>, 2017.
- 755 Emde, C., Buras-Schnell, R., Kylling, A., Mayer, B., Gasteiger, J., Hamann, U., Kylling, J., Richter, B., Pause, C., Dowling, T., and Bugliaro, L.: The libRadtran software package for radiative transfer calculations (version 2.0.1), *Geoscientific Model Development*, 9, 1647–1672, <https://doi.org/10.5194/gmd-9-1647-2016>, 2016.
- Engerer, N. and Mills, F.: KPVI: A clear-sky index for photovoltaics, *Solar Energy*, 105, 679–693, <https://doi.org/10.1016/J.SOLENER.2014.04.019>, 2014.
- 760 Evans, D. and Florschütz, L.: Cost studies on terrestrial photovoltaic power systems with sunlight concentration, *Solar Energy*, 19, 255–262, [https://doi.org/10.1016/0038-092X\(77\)90068-8](https://doi.org/10.1016/0038-092X(77)90068-8), 1977.
- Faiman, D.: Assessing the Outdoor Operating Temperature of Photovoltaic Modules, *Progress in Photovoltaics: Research and Applications*, 16, 307–315, <https://doi.org/10.1002/pip.813>, 2008.
- Frank, C. W., Wahl, S., Keller, J. D., Pospichal, B., Hense, A., and Crewell, S.: Bias correction of a novel European reanalysis data set for
765 solar energy applications, *Solar Energy*, 164, 12–24, <https://doi.org/10.1016/j.solener.2018.02.012>, 2018.
- Halilovic, S., Bright, J. M., Herzberg, W., and Killinger, S.: An analytical approach for estimating the global horizontal from the global tilted irradiance, *Solar Energy*, 188, 1042–1053, <https://doi.org/10.1016/J.SOLENER.2019.06.027>, 2019.
- Herman-Czezuch, A., Mekeng, A. Z., Meilinger, S., Barry, J., and Kimiaie, N.: Impact of aerosols on photovoltaic energy production using a spectrally resolved model chain: Case study of southern West Africa, *Renewable Energy*,
770 <https://doi.org/https://doi.org/10.1016/j.renene.2022.04.166>, 2022.
- Hess, M., Koepke, P., and Schult, I.: Optical properties of aerosols and clouds, *Bull. Amer. Meteor. Soc.*, 79, 831–844, [https://doi.org/10.1175/1520-0477\(1998\)079<0831:OPOAAC>2.0.CO;2](https://doi.org/10.1175/1520-0477(1998)079<0831:OPOAAC>2.0.CO;2), 1998.
- Holben, B. N., Eck, T. F., Slutsker, I., Tanré, D., Buis, J. P., Setzer, A., Vermote, E., Reagan, J. A., Kaufman, Y. J., Nakajima, T., Lavenu, F., Jankowiak, I., and Smirnov, A.: AERONET—A Federated Instrument Network and Data Archive for Aerosol Characterization, *Remote
775 Sensing of Environment*, 66, 1–16, [https://doi.org/https://doi.org/10.1016/S0034-4257\(98\)00031-5](https://doi.org/https://doi.org/10.1016/S0034-4257(98)00031-5), 1998.
- Hu, Y. X. and Stamnes, K.: An Accurate Parameterization of the Radiative Properties of Water Clouds Suitable for Use in Climate Models, *Journal of Climate*, 6, 728–742, [https://doi.org/10.1175/1520-0442\(1993\)006<0728:AAPOTR>2.0.CO;2](https://doi.org/10.1175/1520-0442(1993)006<0728:AAPOTR>2.0.CO;2), 1993.
- Huld, T., Friesen, G., Skoczek, A., Kenny, R. P., Sample, T., Field, M., and Dunlop, E. D.: A power-rating model for crystalline silicon PV modules, *Solar Energy Materials and Solar Cells*, 95, 3359–3369, <https://doi.org/10.1016/j.solmat.2011.07.026>, 2011.
- 780 Kato, S., Ackerman, T. P., Mather, J. H., and Clothiaux, E. E.: The k-distribution method and correlated-k approximation for a short-wave radiative transfer model, *Journal of Quantitative Spectroscopy and Radiative Transfer*, 62, 109–121, [https://doi.org/10.1016/S0022-4073\(98\)00075-2](https://doi.org/10.1016/S0022-4073(98)00075-2), 1999.
- Killinger, S., Braam, F., Müller, B., Wille-Haussmann, B., and McKenna, R.: Projection of power generation between differently-oriented PV systems, *Solar Energy*, 136, 153–165, <https://doi.org/10.1016/J.SOLENER.2016.06.075>, 2016.
- 785 King, D. L., Boyson, W. E., and Kratochvil, J. A.: Photovoltaic array performance model, Tech. Rep. December, Sandia National Laboratories, <https://doi.org/10.2172/919131>, 2004.
- King, D. L., Gonzalez, S., Galbraith, G. M., and Boyson, W. E.: Performance Model for Grid-Connected Photovoltaic Inverters, Tech. Rep. September, <http://jsedres.sepmonline.org/content/38/2/655.abstract>, 2007.
- Klein, S.: Calculation of the monthly-average transmittance-absorptance product, *Solar Energy*, 23, 547–551, [https://doi.org/10.1016/0038-092X\(79\)90083-5](https://doi.org/10.1016/0038-092X(79)90083-5), 1979.
- 790



- Klüser, L., Killius, N., and Gesell, G.: APOLLO_NG - a probabilistic interpretation of the APOLLO legacy for AVHRR heritage channels, *Atmos. Meas. Tech.*, 8, 4155–4170, <https://doi.org/10.5194/amt-8-4155-2015>, 2015.
- Kriebel, K. T., Gesell, G., Kaßner, M., and Mannstein, H.: The cloud analysis tool APOLLO: Improvements and validations, *International Journal of Remote Sensing*, 24, 2389–2408, <https://doi.org/10.1080/01431160210163065>, 2003.
- 795 Laudani, A., Fulginei, F. R., Salvini, A., Carrasco, M., and Mancilla-David, F.: A fast and effective procedure for sensing solar irradiance in photovoltaic arrays, in: 2016 IEEE 16th International Conference on Environment and Electrical Engineering (EEEIC), pp. 1–4, <https://doi.org/10.1109/EEEIC.2016.7555541>, 2016.
- Leontyeva, E. and Stamnes, K.: Estimations of Cloud Optical Thickness from Ground-Based Measurements of Incoming Solar Radiation in the Arctic, *Journal of Climate*, 7, 566–578, [https://doi.org/10.1175/1520-0442\(1994\)007<0566:EOCOTF>2.0.CO;2](https://doi.org/10.1175/1520-0442(1994)007<0566:EOCOTF>2.0.CO;2), 1994.
- 800 Marion, B. and Smith, B.: Photovoltaic system derived data for determining the solar resource and for modeling the performance of other photovoltaic systems, *Solar Energy*, 147, 349–357, <https://doi.org/10.1016/J.SOLENER.2017.03.043>, 2017.
- Mayer, B.: Radiative transfer in the cloudy atmosphere, *EPJ Web of Conferences*, 1, 75–99, <https://doi.org/10.1140/epjconf/e2009-00912-1>, 2009.
- Mayer, B. and Kylling, A.: Technical note: The libRadtran software package for radiative transfer calculations - description and examples of use, *Atmos. Chem. Phys.*, 5, 1855–1877, <https://doi.org/10.5194/acp-5-1855-2005>, 2005.
- 805 Meilinger, S., Herman-Czezuch, A., Kimiaie, N., Schirrmeister, C., Yousif, R., Geiss, S., Scheck, L., Weissmann, M., Gödde, F., Mayer, B., Zinner, T., Barry, J., Pfeilsticker, K., Kraiczky, M., Winter, K., Altayara, A., Reise, C., Rivera, M., Deneke, H., Witthuhn, J., Betcke, J., Schroedter-Homscheidt, M., Hofbauer, P., and Rindt, B.: Entwicklung innovativer satellitengestützter Methoden zur verbesserten PV-Ertragsvorhersage auf verschiedenen Zeitskalen für Anwendungen auf Verteilnetzebene BT - Schlussbericht, Tech. rep., <https://doi.org/https://doi.org/10.18418/opus-5955>, 2021.
- Mertens, K.: *Photovoltaics: Fundamentals, Technology and Practice*, John Wiley & Sons Ltd, first edn., 2014.
- Nakajima, T. and King, M. D.: Determination of the Optical Thickness and Effective Particle Radius of Clouds from Reflected Solar Radiation Measurements. Part I: Theory, *Journal of the Atmospheric Sciences*, 47, 1878–1893, [https://doi.org/10.1175/1520-0469\(1990\)047<1878:DOTOTA>2.0.CO;2](https://doi.org/10.1175/1520-0469(1990)047<1878:DOTOTA>2.0.CO;2), 1990.
- 815 Nespoli, L. and Medici, V.: An unsupervised method for estimating the global horizontal irradiance from photovoltaic power measurements, *Solar Energy*, 158, 701–710, <https://doi.org/10.1016/J.SOLENER.2017.10.039>, 2017.
- Ohmura, A., Dutton, E. G., Forgan, B., Fröhlich, C., Gilgen, H., Hegner, H., Heimo, A., König-Langlo, G., McArthur, B., Müller, G., Philipona, R., Pinker, R., Whitlock, C. H., Dehne, K., and Wild, M.: Baseline Surface Radiation Network (BSRN/WCRP): New Precision Radiometry for Climate Research, *Bulletin of the American Meteorological Society*, 79, 2115–2136, [https://doi.org/10.1175/1520-0477\(1998\)079<2115:BSRNBW>2.0.CO;2](https://doi.org/10.1175/1520-0477(1998)079<2115:BSRNBW>2.0.CO;2), 1998.
- 820 Perez, R., Ineichen, P., Maxwell, E., Seals, R., and Zelenka, A.: Dynamic global-to-direct irradiance conversion model, in: *ASHRAE Transactions*, pp. 354–369, 1992.
- Petty, G. W.: *A First Course in Atmospheric Radiation*, Sundog Publishing, Madison, Wisconsin, second edn., 2006.
- Qu, Z., Oumbe, A., Blanc, P., Espinar, B., Gesell, G., Gschwind, B., Klüser, L., Lefèvre, M., Saboret, L., Schroedter-Homscheidt, M., and Wald, L.: Fast radiative transfer parameterisation for assessing the surface solar irradiance: The Heliosat-4 method, *Meteorologische Zeitschrift*, 26, 33–57, <https://doi.org/10.1127/metz/2016/0781>, 2017.
- Rhodes, B.: *PyEphem: Scientific-grade astronomy routines for Python*, <https://github.com/brandon-rhodes/pyephem>, 2022.



- Rivera Aguilar, M. J. and Reise, C.: Silicon Sensors vs. Pyranometers – Review of Deviations and Conversion of Measured Values, in: 37th European Photovoltaic Solar Energy Conference and Exhibition, pp. 1449 – 1454, Online, <https://doi.org/10.4229/EUPVSEC20202020-5BV.3.3>, 2020.
- 830
- Rodgers, C. D.: Inverse Methods for Atmospheric Sounding, vol. Volume 2, WORLD SCIENTIFIC, <https://doi.org/doi:10.1142/3171>, 2000.
- Saint-Drenan, Y.-M.: A Probabilistic Approach to the Estimation of Regional Photovoltaic Power Generation using Meteorological Data Application of the Approach to the German Case, Dissertation, University of Kassel, <http://nbn-resolving.de/urn:nbn:de:hebis:34-2016090550868>, 2015.
- 835
- Saint-Drenan, Y. M., Bofinger, S., Fritz, R., Vogt, S., Good, G. H., and Dobschinski, J.: An empirical approach to parameterizing photovoltaic plants for power forecasting and simulation, *Solar Energy*, 120, 479–493, <https://doi.org/10.1016/j.solener.2015.07.024>, 2015.
- Sauer, D. U.: Untersuchungen zum Einsatz und Entwicklung von Simulationsmodellen für die Auslegung von Photovoltaik-Systemen, Diplomarbeit, Technische Hochschule Darmstadt, <https://doi.org/10.13140/RG.2.1.1833.7366>, 1994.
- Schade, N. H., Macke, A., Sandmann, H., and Stick, C.: Enhanced solar global irradiance during cloudy sky conditions, *Meteorologische Zeitschrift*, 16, 295–303, <https://doi.org/10.1127/0941-2948/2007/0206>, 2007.
- 840
- Schroedter-Homscheidt, M., Azam, F., Betcke, J., Hanrieder, N., Lefèvre, M., Saboret, L., and Saint-Drenan, Y.: Surface solar irradiance retrieval from MSG/SEVIRI based on APOLLO Next Generation and HELIOSAT-4 methods, *Meteorologische Zeitschrift*, 31, 455–476, <https://doi.org/10.1127/metz/2022/1132>, 2022.
- Scolari, E., Sossan, F., and Paolone, M.: Photovoltaic-model-based solar irradiance estimators: Performance comparison and application to maximum power forecasting, *IEEE Transactions on Sustainable Energy*, 9, 35–44, <https://doi.org/10.1109/TSTE.2017.2714690>, 2018.
- 845
- Shockley, W.: The theory of p-n junctions in semiconductors and p-n junction transistors, *The Bell System Technical Journal*, 28, 435–489, <https://doi.org/10.1002/j.1538-7305.1949.tb03645.x>, 1949.
- Sjerps-Koomen, E. A., Alsema, E. A., and Turkenburg, W. C.: A simple model for PV module reflection losses under field conditions, *Solar Energy*, 57, 421–432, [https://doi.org/10.1016/S0038-092X\(96\)00137-5](https://doi.org/10.1016/S0038-092X(96)00137-5), 1996.
- 850
- Skoplaki, E. and Palyvos, J.: On the temperature dependence of photovoltaic module electrical performance: A review of efficiency/power correlations, *Solar Energy*, 83, 614–624, <https://doi.org/10.1016/J.SOLENER.2008.10.008>, 2009.
- Stamnes, K., Tsay, S.-C., Wiscombe, W., and Jayaweera, K.: Numerically stable algorithm for discrete-ordinate-method radiative transfer in multiple scattering and emitting layered media, *Applied Optics*, 27, 2502, <https://doi.org/10.1364/AO.27.002502>, 1988.
- Stephens, G. L., Ackerman, S., and Smith, E. A.: A Shortwave Parameterization Revised to Improve Cloud Absorption, *Journal of Atmospheric Sciences*, 41, 687–690, [https://doi.org/10.1175/1520-0469\(1984\)041<0687:ASPRTI>2.0.CO;2](https://doi.org/10.1175/1520-0469(1984)041<0687:ASPRTI>2.0.CO;2), 1984.
- 855
- TamizhMani, G., Ji, L., Tang, Y., Petacci, L., and Osterwald, C.: Photovoltaic Module Thermal/Wind Performance: Long-Term Monitoring and Model Development for Energy Rating, NCPV and Solar Program Review Meeting Proceedings, 24-26 March 2003, Denver, Colorado (CD-ROM), <https://www.osti.gov/biblio/15006842>, 2003.
- Urraca, R., Huld, T., Gracia-Amillo, A., Martinez-de Pison, F. J., Kaspar, F., and Sanz-Garcia, A.: Evaluation of global horizontal irradiance estimates from ERA5 and COSMO-REA6 reanalyses using ground and satellite-based data, *Solar Energy*, 164, 339–354, <https://doi.org/10.1016/j.solener.2018.02.059>, 2018.
- 860
- Yang, D. and Bright, J. M.: Worldwide validation of 8 satellite-derived and reanalysis solar radiation products: A preliminary evaluation and overall metrics for hourly data over 27 years, *Solar Energy*, 210, 3–19, <https://doi.org/https://doi.org/10.1016/j.solener.2020.04.016>, 2020.
- Zubler, E. M., Lohmann, U., Lüthi, D., and Schär, C.: Intercomparison of aerosol climatologies for use in a regional climate model over Europe, *Geophysical Research Letters*, 38, <https://doi.org/10.1029/2011GL048081>, 2011.
- 865